

# GRAIN PHYSICS AND IR DUST EMISSION IN AGN ENVIRONMENTS

BRANDON S. HENSLEY

Department of Astrophysical Sciences, Princeton University, Princeton, NJ 08544, USA

JEREMIAH P. OSTRICKER

Department of Astrophysical Sciences, Princeton University, Princeton, NJ 08544, USA and  
 Department of Astronomy, Columbia University, New York, NY 10027, USA

LUCA CIOTTI

Department of Physics and Astronomy, University of Bologna, via Ranzani 1, I-40127, Bologna, Italy

(Dated: February 27, 2014)  
*Draft version February 27, 2014*

## ABSTRACT

We study the effects of a detailed treatment of dust physics on the properties and evolution of early-type galaxies containing central black holes, as determined by AGN feedback. We find that during cooling flow episodes, radiation pressure on the dust in and interior to infalling shells of cold gas can greatly impact the amount of gas able to be accreted and therefore the frequency of AGN bursts. However, the overall hydrodynamic evolution of all models, including mass budget, is relatively robust to the assumptions on dust. Our most detailed models find that the dust to metals ratio is reduced by factors of  $\approx 10^{-1} - 10^{-2}$  relative to Milky Way abundances, and in quiescent phases the dust content of the galaxy would result in  $\sim 0.03$  magnitudes of extinction to the center of the galaxy. We find that IR re-emission from hot dust can dominate the bolometric luminosity of the galaxy during the early stages of an AGN burst, reaching values in excess of  $10^{46}$  erg/s. The AGN-emitted UV is largely absorbed, but the optical depth in the IR does not exceed unity, so the radiation momentum input never exceeds  $L_{\text{BH}}/c$ . We constrain the viability of our models by comparing the energy output in each band, AGN duty cycle, FIR emission, dust mass and opacity, black hole mass, and other model predictions to current observations. These constraints force us to models wherein the destruction of dust in hot gas by sputtering and the competing growth of dust in cold gas results in depletion at the  $\approx 10^{-2}$  level, and only models with a dynamic dust to gas ratio are able to produce both quiescent galaxies consistent with observations and high obscured fractions during AGN “on” phases. During AGN outbursts, we predict that a large fraction of the FIR luminosity can be attributed to warm dust emission ( $\approx 100\text{K}$ ) from dense dusty gas within  $\leq 1\text{kpc}$  reradiating the AGN UV emission.

## 1. INTRODUCTION

It is well-established that the brightest active galactic nuclei (AGNs) and the most massive black holes reside in giant elliptical galaxies. It is also accepted that the environment provided by the galaxy, particularly the abundance of hot metal-rich gas, aging stars, and heavily depleted dust, profoundly affects the supermassive black hole (hereafter SMBH) evolution, and in turn the host system is modified by radiative and mechanical feedback (Begelman et al. 1984; Norman & Scoville 1988; Ciotti & Ostriker 1997, 2012; Ostriker et al. 2010; Pellegrini et al. 2012; Vogelsberger et al. 2013, and references therein). Indeed, the interplay between the evolution of the black hole and the evolution of its host galaxy has been frequently invoked in order to explain the observed correlation between the properties of the black hole and the galaxy (e.g. Springel et al. 2005; Ostriker & Ciotti 2005; Cattaneo et al. 2009; Debuhr et al. 2011). Putting the questions we seek to answer in concrete terms: if the black hole in a galaxy such as M87 were to erupt as a quasar, what would we see? What mechanisms would govern the interaction between the accreting gas of the

galaxy and the erupting black hole? What sources will contribute to the observed radiation?

A key ingredient in answering each of the above questions is the presence of dust in the galaxy. The potential importance of dust can be readily seen for several reasons. First, quasars emit at or near their Eddington limit, which classically is set by the Thomson scattering opacity of  $0.4\text{ cm}^2/\text{g}$ . By comparison, the opacity of dust grains to UV photons exceeds 1000 times this value, so the radiative forces on dust can easily overwhelm other dynamical drivers during outbursts. Second, it is widely accepted that a significant fraction of quasars are obscured. However, the giant elliptical galaxies which host AGN typically have very small optical depths, implying little dust. Therefore, not only does the dust govern the observed radiation from the galaxy, but the dust abundance itself may be a dynamic quantity that evolves in parallel with quasar “on” and “off” phases. In this work, we seek to understand the power of dust to influence the nature, evolution, and observational signatures of giant elliptical galaxies by introducing the processes that create and destroy dust within galaxies into our simulations.

One of the primary links between an AGN and its host galaxy is the immense radiative output of the AGN. The

radiative feedback mechanisms between the central black hole and the accreting gas greatly influence the gas dynamics and thus have been the focus of much study (Binney & Tabor 1995; Ciotti & Ostriker 1997; Thompson et al. 2005; Ciotti & Ostriker 2007, hereafter CO07). Because dust grains efficiently absorb UV radiation and re-radiate in the IR, the presence of grains can dramatically affect the gas dynamics (Siebenmorgen & Heymann 2011, and references therein). In particular, infalling shells of cold gas (a common feature at the onset of ISM cooling episodes and detected in giant ellipticals (Werner et al. 2013)) can be supported by radiation pressure, slowing accretion, and altering the subsequent evolution. In turn, this evolution is related to the so-called “positive feedback” mode in which feedback from the AGN enhances star formation (CO07, Nayakshin & Zubovas 2012, and references therein). Observations have hinted at the presence of radiation-supported cold gas around AGN (Vasudevan et al. 2013) though in the majority ( $\simeq 95\%$ ) of cases the gas is below its effective Eddington limit (Raimundo et al. 2010). Nevertheless, the latter authors note the inevitability of radiation-supported gas and its possible role in AGN feedback. Radiation pressure on dust grains may be instrumental in driving galactic winds (Coker et al. 2013), though there is disagreement as to whether this could be a substantial effect (Socrates & Sironi 2013).

In a recent series of papers (Ciotti et al. 2009b; Shin et al. 2010; Ciotti et al. 2010), 1D hydrodynamical simulations were used to study the mechanisms of AGN feedback. The dust physics was implemented in a very simple, phenomenological way. As sputtering effectively destroys dust in regions of hot gas (Draine & Salpeter 1979), these previous papers approximated the sputtering by reducing the dust to gas ratio in hot gas by roughly two orders of magnitude relative to Galactic values in accord with observations of dust in elliptical galaxies. In practice, a factor inversely proportional to the gas temperature multiplies the fiducial absorption coefficient in the UV, optical, and IR.

In this paper, we improve significantly this aspect of the input physics. We seek to clarify the role of dust grains in AGN feedback by developing and numerically implementing the basic equations for dust production and destruction. For the present hydrodynamical simulations we use an updated version of the 1D code used in our previous studies, with the relevant modifications detailed in Section 3. In particular, a major upgrade has been made in the solution of the radiative transfer equation. We note that in a recent related paper (Novak et al. 2012) the new “two-streams” approach is also tested in the context of 2D hydrodynamical simulations.

We restrict our focus to the secular evolution of the galaxy. While processes such as major and minor mergers or inflows of cold gas from the IGM certainly occur and can account for a variety of observations, we are most interested in which aspects of the evolution of these galaxies can be accounted for by purely secular processes, i.e. driven by well-understood stellar evolutionary processes. We find that the AGN duty cycle, its time dependence, the black hole mass, and the IR luminosity are all naturally explained with our purely secular model.

The paper is organized as follows: in Section 2 we describe the dust grain physics employed in our simulations

as well as a discussion of two-stream radiative transfer. In Section 3 we describe the suite of simulations conducted under different models for the grain abundance. In Section 4, we summarize the results of the simulations and compare against observations to select the most viable models. We also discuss the effects of dust on the properties of AGN outbursts. We then discuss the most viable models in the context of observations in Section 5, focusing on both observational signatures predicted by our model as well as how current observations constrain the survival, growth, and radiative properties of dust in elliptical galaxies with AGN. We summarize the implications of these comparisons in Section 6.

## 2. GRAIN PHYSICS

In this Section we summarize the dust physics implemented in the new version of the code and used for the hydrodynamic simulations.

To aid comparisons between models, we define the factor  $D$  to describe how much the dust is depleted relative to what is observed in the Galaxy, i.e.

$$D \equiv \frac{Z_{\text{MW}}}{Z} \left( \frac{\rho_d}{\rho} \right) \left( \frac{\rho_d}{\rho} \right)^{-1}_{\text{MW}}, \quad (1)$$

where  $\rho$  and  $\rho_d$  are the gas and dust mass densities, respectively, and  $Z$  and  $Z_{\text{MW}}$  are the metallicities of the simulated galaxy and the Milky Way, respectively. This is motivated by the fact that the dust to gas ratio of a galaxy should scale linearly with the metallicity. A depletion factor of 1 therefore indicates that the fraction of metals incorporated in dust grains is the same as in the Milky Way. We adopt  $Z_{\text{MW}} = Z_{\odot}$ , a Galactic dust to gas ratio of 0.01, and  $Z/Z_{\text{MW}} = 4/3$ .

### 2.1. Grain Opacity

Following CO07, we adopt the dust opacity values

$$\kappa_{\text{opt}} = 300 \left( \frac{Z}{Z_{\text{MW}}} \right) \times D, \quad \kappa_{\text{UV}} = 4\kappa_{\text{opt}}, \quad \kappa_{\text{IR}} = \frac{\kappa_{\text{opt}}}{150}, \quad (2)$$

i.e. dependent on the dust to gas ratio in the galaxy relative to the Milky Way. Note that in CO07,

$$D = \frac{1}{1 + T_4}, \quad (3)$$

where  $T_4$  is the gas temperature in units of  $10^4$  K and the metallicity taken to be  $Z_{\odot}$ . For coronal X-ray emitting gas in a typical elliptical galaxy, this corresponds to a depletion factor of  $\simeq 10^{-2}$ . In the following, we present a method for computing  $D$  in a much more physically consistent way than Equation 3.

### 2.2. Dust Abundance

The primary source of dust in galaxies is the massive winds ejected by dying AGB stars during thermal pulses (for example as planetary nebulae) and by supernova explosions. The ultimate fate of these winds is not fully understood, but it is commonly accepted that some form of mixing and thermalization with the preexisting ISM takes place on short timescales (e.g. Bregman & Parricott 2009). Therefore, it is natural to expect that the

dust is transported through the galaxy by the large scale gas flows of early type galaxies (Kim & Pellegrini 2012), where it is sputtered by the hot ISM and, in cold gas, allowed to grow via collisions with metal atoms. Moreover, when dust-bearing gas forms new stars, the dust is removed from the ISM and sequestered into the stars.

In the previous simulations discussed in the Introduction, these effects were addressed qualitatively by assuming that the cold gas was grain-rich and the hot gas was grain-poor. In practice, this was implemented by approximating the dust to gas ratio at each radius by Equation (3). However, this prescription changes the dust abundance instantaneously with temperature and does not allow for the transport of grains from one radius to another.

### 2.2.1. One Component Model

The new treatment addresses both issues by implementing a grain continuity equation

$$\frac{\partial \rho_d}{\partial t} + \nabla \cdot (\rho_d \mathbf{v}) = S_+ - S_-, \quad (4)$$

where  $\rho_d$  is the mass density of dust grains. Note that  $\mathbf{v}$  is the gas velocity given by the hydrodynamic code since for simplicity we assume that the grains are coupled to the motion of the gas; finally  $S_+$  and  $S_-$  are the dust source and sink terms, respectively. As discussed below, each of the two functions  $S_+$  and  $S_-$  is in turn given by the sum of two terms. We term this the “One Component” model as all dust in this model is assumed to be mixed with the ISM. We describe a “Two Component” model in Section 2.2.2 that considers mixed and unmixed dust separately.

In the Milky Way, the dust to gas ratio in outflows of oxygen-rich AGB stars has been observed to be  $\simeq 0.0063$  (Knapp 1985; Kemper et al. 2003). Since an early type galaxy can be metal-enriched relative to the Milky Way, we adopt a fiducial dust to gas mass ratio of 0.01 in these outflows, and the source term is simply

$$S_{+,inj} = 0.0133\dot{\rho}_*, \quad (5)$$

where  $\dot{\rho}_*$  is the gas released by stars as described in CO07 Equation 13, and the numerical factor is dimensionless.

In the particularly hot ISM of elliptical galaxies, grains are rapidly sputtered. To compute the dust destruction rate due to sputtering, we use the relation

$$\dot{a} = -\frac{10^{-6}n_H}{1 + T_6^{-3}} \mu\text{m yr}^{-1} \quad (6)$$

where  $a$  is the grain radius,  $T_6$  is the gas temperature in units of  $10^6$  K, and  $n_H$  is the proton number density in units of  $\text{cm}^{-3}$ . This expression is a good approximation for graphite and silicate grains in gas with  $10^5 < T < 10^9$  K (Draine 2011); note that  $\dot{a}$  is independent of  $a$ . Empirically, the size distribution of dust grains above  $\simeq 50\text{\AA}$  can be approximated by the standard Mathis-Rumpl-Nordsieck (MRN) distribution (Mathis et al. 1977) despite destruction and creation processes. Therefore, we assume that the MRN distribution is valid at all times, i.e.

$$\frac{dn_d}{da} = \frac{H a_{\max}^{2.5}}{a^{3.5}} \quad (7)$$

is the number density of grains with size between  $a$  and  $a+da$ , where  $H$  is a normalization constant, in principle dependent on time and position in the galaxy. In the following, we assume  $a_{\min} = 0.005\mu\text{m}$  and  $a_{\max} = 0.3\mu\text{m}$ . The total density in grains at a given radius and time is then

$$\rho_d \simeq \frac{8\pi}{3} H \rho_{\text{grain}} a_{\max}^3, \quad (8)$$

where  $\rho_{\text{grain}}$  is the internal density of a dust grain and we neglected the factor of  $1 - \sqrt{a_{\min}/a_{\max}}$ . We take  $\rho_{\text{grain}} = 3.5 \text{ g cm}^{-3}$  which is a standard value for silicate grains. The total destruction rate is obtained by computing the mass destruction rate of grains of radius  $a$  and then integrating over the distribution. It follows that

$$\dot{\rho}_{d,gd} = 8\pi H \rho_{\text{grain}} \left( \frac{a_{\max}}{a_{\min}} \right)^{0.5} a_{\max}^2 \dot{a}, \quad (9)$$

and from Eqs. (8)-(9), we can define a grain destruction frequency

$$\nu_{gd} \equiv \frac{|\dot{\rho}_{d,gd}|}{\rho_d} = 3 \left( \frac{a_{\max}}{a_{\min}} \right)^{0.5} \frac{|\dot{a}|}{a_{\max}}. \quad (10)$$

Therefore, the sputtering term in Equation 4 is

$$S_{-,gd} = \nu_{gd} \rho_d. \quad (11)$$

Note that in principle, in AGN environments, where high energy photons can ionize grains, the sputtering time can be altered by the effects of grain charging. However, Weingartner et al. (2006) find that the effect at  $r = 100 \text{ pc}$  for an  $L_{\text{BH}} = 10^{46} \text{ erg/s}$  quasar is negligible above  $\simeq 10^6 \text{ K}$ , even for large ionization parameters. Thus, this effect may be safely neglected.

In cold gas, metal atoms are able to collide with dust grains and stick. If these metal atoms have a probability  $f$  of sticking and are moving with average speed  $v_Z$ , then the source term due to these collisions is  $f \rho_Z v_Z 4\pi a^2 n_d$ , where  $\rho_Z = f_Z \rho$  is the mass density of the metals and  $f_Z$  is the mass fraction of gas available for making grains. If we assume that the Milky Way has included all such materials in grains already, then  $f_Z$  for the Milky Way would just be its observed dust to gas ratio of 0.01. Since the simulated galaxy has a metallicity 4/3 greater than the Milky Way, we take  $f_Z$  to be 0.0133. However, grain growth cannot continue after the metals in the gas have been used up, so we replace  $f_Z$  with  $f_Z - \rho_d/\rho$  to disallow growth beyond the available metal atoms. Integrating this over the grain size distribution, we obtain

$$\dot{\rho}_{d,gg} = f \rho \frac{c_s}{\sqrt{\mu_Z}} 8\pi \left( f_Z - \frac{\rho_d}{\rho} \right) H a_{\max}^2 \left( \frac{a_{\max}}{a_{\min}} \right)^{0.5}, \quad (12)$$

where we have made the approximation  $v_Z = c_s/\sqrt{\mu_Z}$ , with  $c_s$  being the sound speed in the gas and  $\mu$  the mean atomic mass of the metal atoms. We adopt the values  $f = 0.2$  and  $\mu_Z = 16$ . Thus the grain growth frequency is

$$\nu_{gg} \equiv \frac{\dot{\rho}_{d,gg}}{\rho_d} = \frac{3f\rho c_s}{\rho_{\text{grain}} a_{\text{max}} \sqrt{\mu Z}} \left( f_Z - \frac{\rho_d}{\rho} \right) \left( \frac{a_{\text{max}}}{a_{\text{min}}} \right)^{0.5}. \quad (13)$$

The ratio of grain growth by collisions to sputtering is a temperature dependent function given by

$$\frac{\nu_{gg}}{\nu_{gd}} = 1.18 \times 10^{-6} (1 + T_6^{-3}) \sqrt{T} \quad (14)$$

for our assumed galaxy parameters and approximating  $f_Z \gg \rho_d/\rho$ . Figure 1 plots the growth and destruction times as a function of temperature for gas with  $n_H = 0.1 \text{ cm}^{-3}$ . Grain growth is negligible in all but the coldest gas.

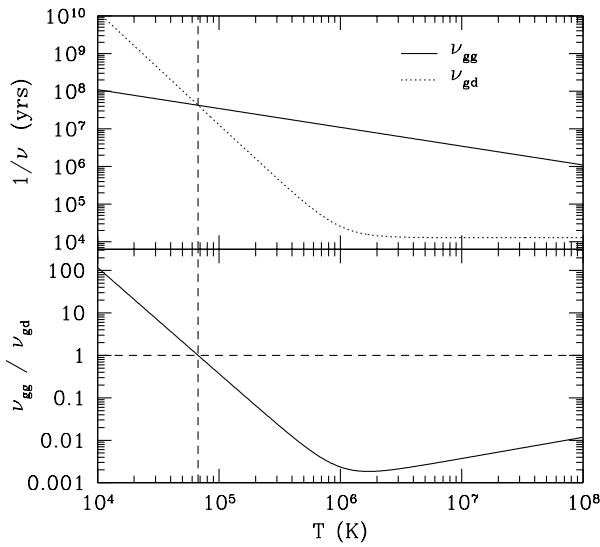


FIG. 1.— *Top*: Grain growth (Equation 13) and destruction (Equation 10) times for a representative value  $n_H = 0.1 \text{ cm}^{-3}$  and  $f_Z \gg \rho_d/\rho$ . Net grain growth will only occur in gas colder than  $\simeq 7 \times 10^4 \text{ K}$ . Note that for these temperatures, grain growth time can be as short as  $10^4$  years for a density of  $10^3 \text{ cm}^{-3}$  (see Figure 9) due to the linear dependence of the growth frequency on density. *Bottom*: The ratio of the growth to destruction frequencies (Equation 14).

Finally, grains will be removed from the ISM when the gas containing those grains form stars. The star formation rate  $\dot{\rho}_*^+$  is given in CO07 (Equation 15), allowing us to compute the dust destruction due to star formation as

$$S_{-,SF} = \frac{\rho_d}{\rho_g} \dot{\rho}_*^+ \quad (15)$$

Combining the equations in this section, we now have the expression for the dust source and sink terms:

$$S_+ - S_- = S_{+,inj} + S_{+,gg} - (S_{-,gd} + S_{-,SF}). \quad (16)$$

By evolving Equation 4 for each position and time, we can evaluate the D function in Equation 1 with the computed value of  $\rho_d$ .

### 2.2.2. Two Component Model

The one component approach assumes that dust mixes with gas instantaneously after its creation in stellar outflows. However, stellar ejecta contains dust not yet mixed with the ambient ISM. Although dust-laden, these compact planetary nebulae will not contribute significantly to the total infrared opacity of the galaxy. Therefore, the mixing process introduces a lag time between dust creation and its consequent effects on the radiative feedback in the galaxy.

To estimate the mixing time, we consider a planetary nebula of mass  $\Delta M$  expanding with velocity  $v_1$  relative to the parent star into a surrounding medium of density  $\rho_{\text{ext}}$  and sound speed  $c_s$ . We further define  $v_{\text{rel}}$  as an estimate of the relative velocity of the star with respect to the surrounding ISM, so that a fiducial value is the local (1D) velocity dispersion of the stars. We denote the internal density as  $\rho_1$  and the radius of the nebula as  $r_1$ . The nebula expands until it comes into pressure equilibrium with the surrounding medium, i.e.,

$$v_1^2 \rho_1 = P_{\text{ext}} \quad (17)$$

Hence the time to reach pressure equilibrium  $t_{eq}$  is

$$t_{eq} = \left( \frac{3\Delta M}{4\pi v_1 P_{\text{ext}}} \right)^{1/3} \quad (18)$$

Defining the Mach number  $\mathcal{M} \equiv \frac{v_{\text{rel}}}{c_s}$ , the ram pressure experienced by the expanding wind is

$$P_{\text{ext}} = \rho_{\text{ext}} (v_{\text{rel}}^2 + c_s^2) = v_{\text{rel}}^2 \rho_{\text{ext}} (1 + \mathcal{M}^{-2}) \quad (19)$$

Let  $t_{fr}$  be the time it takes the planetary nebula to encounter a gas mass equal to its own mass, thereby fragmenting and mixing it. Then,

$$\frac{\Delta M}{\pi r_1^2} = t_{fr} \rho_{\text{ext}} \max(v_1, v_{\text{rel}}) \quad (20)$$

where typically  $v_{\text{rel}} \gg v_1$ . Using Equation 19,  $t_{fr}$  can be expressed as

$$t_{fr} = \left( \frac{16}{9\pi} \right)^{1/3} (1 + \mathcal{M}^{-2})^{2/3} \left( \frac{v_{\text{rel}}}{v_1} \right)^{1/3} \left( \frac{\Delta M}{v_1^3 \rho_{\text{ext}}} \right)^{1/3} \quad (21)$$

In addition to fragmentation, we must also consider evaporation due to thermal conduction. Following Draine (2011) Equation 34.17,

$$t_{ev} = 1.6 \times 10^3 \text{ yr} \left( \frac{\Delta M}{1 M_\odot} \right) \left( \frac{r_{ev}}{1 \text{ pc}} \right)^{-1} \left( \frac{T}{10^7 \text{ K}} \right)^{-2.5}, \quad (22)$$

where  $T$  is the gas temperature and  $r_{ev}$  is the radius of the nebula when it evaporates. Note that we have assumed that the Coulomb logarithm  $\ln \Lambda = 30$ . In our implementation of these equations,  $\Delta M = 0.1 M_\odot$ , and  $v_1 = 10 \text{ km/s}$ .

There are three distinct regimes to consider. First, consider the case in which  $t_{ev} < t_{eq}$ , i.e. the nebula evaporates before it expands to pressure equilibrium. Then the radius  $r_{ev} = v_1 t_{ev}$ . Solving for  $t_{ev}$ , which in this case is the mixing time, we obtain

$$t_{\text{mix},1} = 8.4 \times 10^3 \text{ yr} \left( \frac{T}{10^7 K} \right)^{-5/4}. \quad (23)$$

However, if  $t_{eq} < t_{ev}$ , then  $r_{ev} = r_1$ . Once at pressure equilibrium, the nebula can mix via fragmentation or evaporation, depending on which is faster. In the former case,

$$t_{\text{mix},2} = 1.5 \times 10^3 \text{ yr} \left( \frac{T}{10^7 K} \right)^{-5/2} \left( \frac{v_{\text{rel}}}{300 \text{ km/s}} \right)^{2/3} \times (1 + \mathcal{M}^{-2})^{1/3}. \quad (24)$$

However, if  $t_{\text{mix},2} > t_{fr}$ , we are in the third regime where the mixing time  $t_{\text{mix},3} = t_{fr}$ :

$$t_{\text{mix},3} = 1.9 \times 10^6 \text{ yr} \left( \frac{v_{\text{rel}}}{300 \text{ km/s}} \right)^{1/3} \left( \frac{n_{\text{H}}}{0.01 \text{ cm}^{-3}} \right)^{-1/3} \times (1 + \mathcal{M}^{-2})^{2/3}. \quad (25)$$

In summary, the mixing time is defined as

$$t_{\text{mix}} = \begin{cases} t_{\text{mix},1}, & t_{ev} < t_{eq}; \\ \min(t_{\text{mix},2}, t_{\text{mix},3}), & t_{ev} > t_{eq}. \end{cases} \quad (26)$$

Equipped with a mixing time, we may now modify the continuity equations for gas and dust by distinguishing between the planetary nebula (PN) and diffuse ISM phases. We assume that no dust growth or destruction occurs in the PN phase.

$$\frac{\partial \rho_{g,ISM}}{\partial t} + \nabla \cdot (\rho_g \mathbf{v}) = \dot{\rho}_{\text{II}} + \frac{\rho_{g,PN}}{t_{\text{mix}}} \quad (27)$$

$$\frac{\partial \rho_{g,PN}}{\partial t} = \dot{\rho}_* - \frac{\rho_{g,PN}}{t_{\text{mix}}} \quad (28)$$

$$\frac{\partial \rho_{d,ISM}}{\partial t} + \nabla \cdot (\rho_d \mathbf{v}) = 0.0133 \dot{\rho}_{\text{II}} + \nu_{gg} \rho_{d,ISM} - \nu_{gd} \rho_{d,ISM} - \quad (29)$$

$$\frac{\partial \rho_{d,PN}}{\partial t} = 0.0133 \dot{\rho}_* - \frac{\rho_{d,PN}}{t_{\text{mix}}}, \quad (30)$$

where  $\dot{\rho}_{\text{II}}$  is the gas source term not associated with planetary nebulae (see CO07 Equation 23).

### 2.3. Grain Temperature

The physics presented in the previous section directly influences the hydrodynamical evolution of the models. Here we present additional physics needed to compute observational properties of the models, the other focus of this work.

By numerical integration of the radiative transfer equations in the one-stream approximation (see Section 2.4), we compute the total radiation density in each shell. We approximate the total radiation absorbed in each radial shell by dust as the difference in luminosity at the base and end of the shell, i.e.

$$\Delta L = L_{\text{eff},\text{inner}} - L_{\text{eff},\text{outer}}. \quad (31)$$

Assuming all grains have the same temperature  $T_d$  and imposing that the total dust emission in a shell of volume  $V$  is equal to the computed  $\Delta L$ , the relation between  $T_d$  and  $\Delta L$  in a given shell is:

$$\Delta L = V \sigma T_d^4 \int_{a_{\text{min}}}^{a_{\text{max}}} da \frac{dn_d}{da} 4\pi a^2 Q(a, T_d), \quad (32)$$

where  $Q(a, T_d)$  is the Planck-averaged emission efficiency. Following Draine (2011), we make the approximation

$$Q(a, T_d) = \begin{cases} \left( \frac{a}{0.1 \mu\text{m}} \right) 1.3 \times 10^{-6} T_d^2, & T_d < 164; \\ \left( \frac{a}{0.1 \mu\text{m}} \right) 3.5 \times 10^{-2}, & T_d > 164; \end{cases} \quad (33)$$

where  $T_d$  is in Kelvin. By inserting Equation 33 into Equation 32, some algebra shows that the equilibrium dust temperature is given by

$$T_d = \begin{cases} 5.97 \left( \frac{\rho_{\text{grain}} \Delta L}{\rho_d V} \right)^{\frac{1}{6}}, & T_d < 164; \\ 1.14 \left( \frac{\rho_{\text{grain}} \Delta L}{\rho_d V} \right)^{\frac{1}{4}}, & T_d > 164; \end{cases} \quad (34)$$

where all quantities are in cgs. Note that the integral in Equation 32 is monotonic in  $T_d$ , therefore ensuring only one branch of Equation 34 is selected for given input values of  $\Delta L$ ,  $V$ , and  $\rho_d$ . Because this calculation neglects the stochastic heating of small grains, the derived grain temperature should be considered as a characteristic temperature for the far infrared (FIR) dust emission.

Finally, we define the luminosity-weighted dust temperature  $\langle T_d \rangle$  to be

$$\langle T_d \rangle = \frac{1}{L_{\text{IR}}} \int T_d(r) L_{\text{IR}}(r) dr, \quad (35)$$

which provides an estimate of the temperature of the dust producing the observed IR emission.

### 2.4. One-Stream Radiative Transfer in Spherical Symmetry

The integration scheme for the radiative transfer equation has been improved with respect to Ciotti et al. (2010). The full description of the new scheme is given in Novak et al. (2012). In particular, we adopt the Simplified Radiation Transport in Section 3.2, which we describe briefly below. In Novak et al. (2012) the full equations of radiative transfer were solved by using a relaxation method, and it was shown that the following approximation works remarkably well for the present problem.

The radiation transport equations for the black hole radiation are particularly simple because all UV and optical photons emitted from the black hole will necessarily be outgoing photons assuming that the scattering opacity is negligible. This yields the relation

$$\frac{dL_{\text{eff},\text{BH}}}{dr} = -\rho \kappa_i L_{\text{eff},\text{BH}}, \quad (36)$$

where  $\kappa_i$  is the dust opacity in band  $i$  and the effective black hole luminosity  $L_{\text{eff,BH}}$  is the outgoing black hole luminosity remaining after absorption.

For other radiation sources, however, the equation is complicated by the fact that photons may be emitted inward toward the center of the galaxy and, providing the optical depth is low enough, re-emerge on the other side as an outgoing photon. To account for this, we approximate the likelihood of an inward-emitted photon becoming an outgoing photon by the function  $\Psi$  which is defined as

$$\Psi \equiv 1 - \frac{0.5}{1 + \exp(-\tau)} \frac{r_1^2}{\max(r_1^2, r^2)} \quad , \quad (37)$$

where  $\tau$  is the optical depth from  $r$  to infinity and  $r_1$  is the radius at which  $\tau = 1$ . Using this parameterization, the radiative transport equation for the outgoing stellar radiation  $L_{\text{eff},*}$  is given by

$$\frac{dL_{\text{eff},*}}{dr} = 4\pi r^2 \Psi \dot{E} - \rho \kappa_i L_{\text{eff},*} \quad , \quad (38)$$

where  $\dot{E}$  is energy radiated by stars per unit volume per unit time.

In addition to the changes detailed in Novak et al. (2012), we also include an updated prescription for the optical depth of a radial shell. If a shell is optically thick, only a portion of the shell will experience a force from the radiation pressure. To achieve the proper limiting behavior, we modify the optical depth in a band  $i$  of a given shell  $\tau'_i$  in the following way to obtain a  $\tau_i$  for use in all calculations:

$$\tau_i \equiv 1 - e^{-\tau'_i} \quad . \quad (39)$$

### 3. SIMULATIONS

For simplicity, we restrict our simulations to the class of Type A models described in Ciotti et al. (2010). In these models, the opening angle of the broad line region (BLR) wind and the mechanical efficiency  $\epsilon_w$  are independent of the accretion luminosity.  $\epsilon_w = 10^{-4}$  is a factor of two below the mechanical efficiency assumed in many of the treatments of AGN feedback, such as Di Matteo et al. (2005), but similar to the value found most appropriate when winds are included (see, e.g., Choi et al. 2013). We note that including the momentum of the outgoing wind makes a given energy input far more effective (Choi et al. 2012).

For ease of comparison, all of the dynamical properties relevant for the simulations is the same as in Ciotti et al. (2009b), i.e. a Jaffe stellar distribution plus a dark matter halo so that the total density profile is proportional to  $1/r^2$ . The total stellar mass of  $3 \times 10^{11} M_\odot$  and effective radius  $R_e = 6.9$  kpc result in a central velocity dispersion  $260 \text{ km s}^{-1}$ . Dynamical properties of the model are given in Ciotti et al. (2009a). The treatment of the physics for the stellar component of the galaxy, including stellar evolution, Type Ia and Type II Supernovae, and star formation, as well as the hydrodynamical equations are fully described in Ciotti & Ostriker (2012). The initial mass of the central SMBH is fixed to  $M_{\text{BH}} = 10^{-3} M_*$  as in previous papers, therefore approximately following the Magorrian relation. In practice, all

of the evolutionary phases of galaxy formation leading to the establishment of the Magorrian relation are not considered. Accretion onto the BH is computed from the full hydrodynamic equations rather than assuming Bondi accretion or other approximate treatments. It is mediated by a circumnuclear accretion disk whose balance equations are integrated as subgrid physics (Ciotti & Ostriker 2012). Each simulation employs 240 cells with the innermost gridpoint at 2.5 pc and the outermost at 208 kpc. As in the previous papers, for simplicity we assume standard outflow boundary conditions at the grid outer boundary and use a dynamic time resolution based on the physical timescales in the galaxy. However, we increase the time resolution by an additional factor of 10 relative to previous work.

In summary, the models are in all respect identical to previous models with the exception of a better treatment of dust, an improved numerical integration of the radiative transfer (see also Novak et al. 2012), and increased spatial and temporal resolution. However, for the same input physics and previous dust treatment, the results are nearly identical to previous ones. Our  $A_2$  model refers to the precise implementation of the same model in Ciotti et al. (2010) as we use Equation 3 to model the dust depletion.

We introduce five variants of the  $A_2$  model - and thus six models in all, with each variant utilizing a different prescription for the dust abundance and distribution. These models are summarized in Table 1, where they are listed in the approximate order of increasing dust to gas ratio at the end of the simulation.

In the first model,  $A_2^{\text{ND}}$ , we consider a galaxy completely devoid of dust, i.e. the depletion factor  $D$  in Equation 1 is fixed to zero.

$A_2^{\text{MW}}$ , with a dust to gas ratio equal to that of the Milky Way scaled to the metallicity of our galaxy ( $Z = 4/3 Z_{\text{MW}}$ ), is the other extreme model. In this maximum dust model,  $D = 1$ .

We have two additional models in which the dust to gas ratio is a fixed number independent of time and position. First is  $A_2^{-4}$ , in which  $\rho_d/\rho = 10^{-4}$  at all radii. This is motivated by recent Herschel observations (Smith et al. 2011) of the dust masses of 62 early type galaxies and scaled to our assumed stellar mass of  $3 \times 10^{11} M_\odot$ . In interest of spanning the viable range of dust to gas ratios, we also introduce  $A_2^{-3}$  in which  $\rho_d/\rho = 10^{-3}$ .

Our most sophisticated models embody the suite of physics for grain production and destruction outlined in Section 2.2 to compute the dust mass density at each radius and the resulting dust opacity. The  $A_2^{\text{CE}}$  model employs the ‘‘One Component’’ formalism of Section 2.2.1 while  $A_2^{\text{CE2}}$  the ‘‘Two Component’’ formalism of Section 2.2.2.

### 4. A FIRST SURVEY OF THE MODELS

We begin by comparing the overall behavior of all models in Table 1. Our purpose is two-fold: first to understand the effects of different treatments of the dust to gas ratio. In particular, Section 4.1 is dedicated to the effects during AGN bursts. Second, we select the subset of models that best corresponds to observations, which we discuss in detail in Section 5.

The first column of Table 1 shows the mass ejected as a galactic wind, illustrating that the bulk of the mass pro-

TABLE 1  
SUMMARY OF MODELS

Model	Depletion	$\Delta M_w$ [ $M_\odot$ ]	$\Delta M_*$ [ $M_\odot$ ]	$M_{\text{gas}}$ [ $M_\odot$ ]	$L_X$ [erg/s]	$\frac{M_{\text{dust}}}{M_{\text{gas}}}$	$\frac{L_{\text{IR}}}{L_{\text{OP}*}}$	$\tau_{\text{OP}}$	$\Delta M_{\text{BH}}$ [ $M_\odot$ ]	$e_{\text{Bol}}$	$e_{\text{UV}}$ $e_{\text{OP}}$	$e_{\text{IR}}$ $e_X$	$N_{\text{burst}}$	$f_{\text{duty}}$
$A_2^{\text{ND}}$	0	10.43	9.40	9.04	38.15	—	—	—	8.97	0.11	0.040 0.029	0.034 0.011	81	-2.21
$A_2$	$1/1+T_4$	10.42	9.26	9.14	38.26	-4.37	-4.75	-5.00	8.65	0.11	0.016 0.013	0.073 0.011	51	-2.45
$A_2^{-4}$	$0.75 \times 10^{-2}$	10.29	9.38	9.91	40.49	-4.06	-3.68	-3.31	8.64	0.11	0.023 0.020	0.058 0.011	46	-2.25
$A_2^{\text{CE}}$	Computed	10.32	9.36	9.83	40.47	-3.88	-3.15	-2.01	8.67	0.11	0.013 0.010	0.079 0.011	57	-2.42
$A_2^{\text{CE}2}$	Computed	10.21	9.98	10.10	40.57	-2.74	-2.65	-1.93	9.01	0.12	0.007 0.005	0.092 0.012	86	-2.20
$A_2^{-3}$	$0.75 \times 10^{-1}$	10.24	10.06	9.38	39.03	-3.06	-3.30	-2.92	8.91	0.12	0.006 0.005	0.091 0.012	76	-2.27
$A_2^{\text{MW}}$	1	10.34	8.19	9.80	39.48	-1.94	-2.07	-1.68	7.79	0.10	0.017 0.020	0.056 0.010	14	-3.14

**Notes:** The models are arranged roughly by dust content, from lowest to highest. All quantities are the values attained at the end of the simulation, which in all cases represents a quiescent giant elliptical galaxy. Depletion is the ratio of dust to metals in the model relative to the dust to metal ratio in the Galaxy (Equation 1);  $\Delta M_{\text{BH}}$  is the total mass accreted by the black hole;  $\Delta M_w$  is the total mass ejected as a galactic wind;  $\Delta M_*$  is the total mass of new stars;  $e_i \equiv \Delta E_i / \Delta M_{\text{BH}} c^2$  is the total energy emitted by the black hole in band  $i$  (as seen from infinity) divided by the energy equivalent of the black hole mass growth;  $L_{\text{IR}}/L_{\text{OP}*}$  is the ratio of the IR luminosity from dust and the effective optical luminosity from stars;  $\tau_{\text{OP}}$  is the optical depth in the optical band;  $L_X$  is the X-ray luminosity of the ISM in the galaxy;  $N_{\text{burst}}$  is the number of burst events; and  $f_{\text{duty}}$  is the the fraction of time spent with  $L_{\text{Bol}} > L_{\text{Edd}}/30$ . All quantities except  $e_i$  and  $N_{\text{burst}}$  given as  $\log_{10}$ .

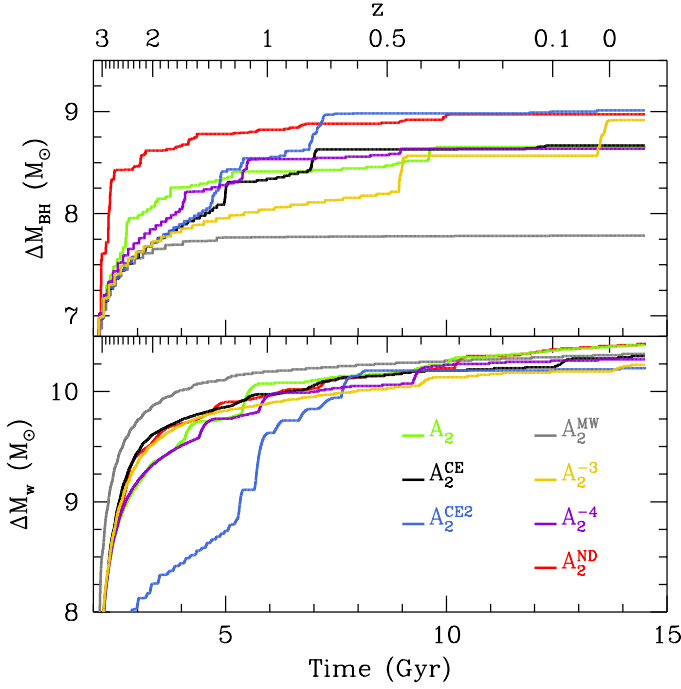


FIG. 2.— *Top:* The black hole mass growth since the beginning of the simulation. *Bottom:* The total mass ejected as a galactic wind. AGN activity peaks at early times ( $z \sim 2-3$ ) in all models, and the black holes are quiescent in all models by the present epoch ( $z \sim 0$ ). All y-axis quantities are given as  $\log_{10}$ .

duced by stellar evolution is ejected as a galactic wind (see also Figure 2). Such galactic winds in our model are supported by thermalization of stellar motion and in particular by heating provided by Type Ia supernovae. Due to the time dependence of the supernovae and star formation, the specific heating rate increases with time. Black hole activity itself is not enough to drive a galactic wind. However, it assists in ejecting gas and in fact

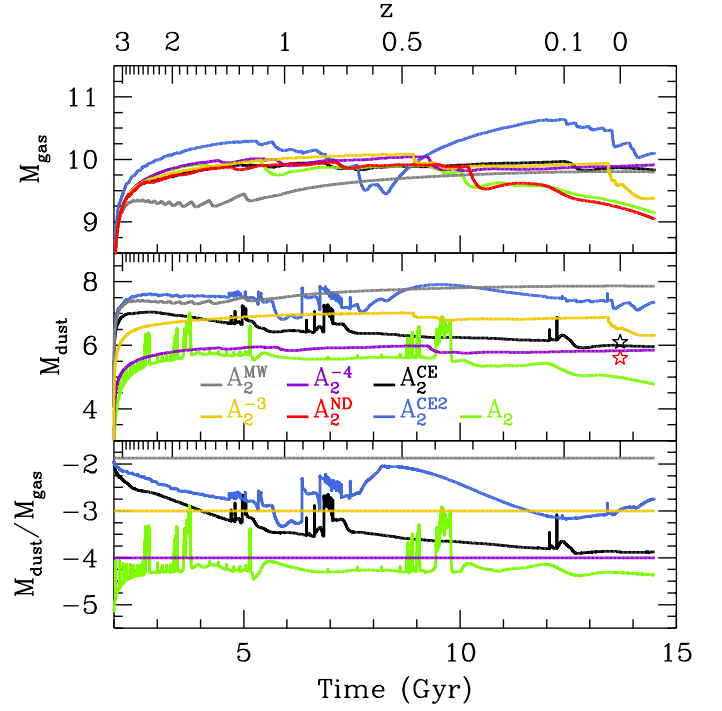


FIG. 3.— *Top:* The total gas content of the galaxy in  $M_\odot$ . The colors are the same as in Figure 2. *Middle:* The total dust content of the galaxy in  $M_\odot$ . Spikes occur during cooling instabilities, leading to the formation of infalling shells prior to outbursts. We plot the average dust mass for early type galaxies as determined by the Herschel Reference Survey (Smith et al. 2011) as a black star (detections only) and red star (including non-detections). *Bottom:* The dust to gas ratio of the galaxy. All y-axis quantities are given as  $\log_{10}$ .

models with larger black holes by the end of the simulation have in general more mass ejected as well. This is due to the fact that larger black holes allow for higher Eddington luminosities.

The next column reports the mass of new stars formed over the simulation. Note that this value is always intermediate between  $\Delta M_{\text{BH}}$  and  $\Delta M_w$ . This fact has important cosmological implications as it clearly shows how Type Ia supernovae are responsible for the metal pollution of the IGM since the bulk of the gas is ejected, not locked into new stars. As already described in CO07, AGN feedback has competing effects on star formation, acting as both positive feedback during bursts and as negative feedback at the end of each burst. This leads to the surprising result that pure cooling flow models may form fewer stars than models with AGN feedback. It is also known that, at least in 1D models, the bulk of star formation happens in a region of about a few hundred parsecs in size where cold shells are formed by recurrent cooling instabilities and shocks induced by AGN feedback. Therefore, we expect a correlation between the number of bursts and the number of new stars formed (see Table 1).

In the next column, we report the total amount of gas in the simulation. Overall, the gas masses are consistent with observations of galaxies with comparable velocity dispersions (Canizares et al. 1987; Kim & Pellegrini 2012).

In the next column is the final X-ray luminosity of the hot gaseous corona of our models obtained by integrating the gas emissivity in the 0.38 keV band within the volume of 10 effective optical radii. For all models, luminosities are in the observed range (Boroson et al. 2011). The low luminosities of models  $A_2^{\text{ND}}$  and  $A_2$ , in conjunction with their low total gas mass, demonstrate that these models are in a global wind phase at the present time. The luminosities of the other models are consistent with inflow/partial wind states. At the end of the simulation, all models are in a state of hot, low-luminosity accretion.

In the next column, we give the dust to gas ratio over the galaxy at the end of the simulation. The models are ordered as expected from the dust physics. By construction,  $A_2^{\text{ND}}$  is inconsistent with observations since it has no dust, and  $A_2^{\text{MW}}$  has too much dust relative to observed giant ellipticals. Additionally,  $A_2^{-3}$  and  $A_2^{\text{CE2}}$  are on the high end of what would be expected (see Section 5.1). However, the enhanced dust content of the  $A_2^{\text{CE2}}$  model is not directly related to the dust treatment, but rather is due to a large star formation episode following the last AGN burst (see bottom panel of Figure 3). More extensive exploration of the  $A_2^{\text{CE2}}$  model is needed to determine if these star formation episodes are a generic feature of the model.

The next column reports the ratio of the IR dust emission from reprocessed optical and UV radiation from stars and the black hole to the total effective luminosity of stars in the optical band. This ratio varies widely between models, and is thus an important observational diagnostic. The ratio has the expected behavior— as the dust abundance increases, the IR luminosity increases and the optical luminosity decreases due to absorption. Thus, the ratio should increase with increasing dust, which is the observed behavior. This trend is also evident in the next column, which gives the optical depth in the optical band to the center of the galaxy. For elliptical galaxies, Smith et al. (2011) find a ratio of FIR to B-band luminosity  $-2.5 < \log L_{\text{FIR}}/L_{\text{B}} < -1.5$  with

a number of upper limits at the lower end of the range. We stress that our  $L_{\text{IR}}/L_{\text{OP*}}$  does not correspond exactly, but we can still make some useful comparisons. If we include upper limits, all models are in agreement. However, when restricting the comparison to detections,  $A_2^{\text{ND}}$  and  $A_2$  are clearly ruled out and  $A_2^{-4}$  and  $A_2^{\text{CE}}$  are only marginally consistent.

In summary, all models produce acceptable results from a hydrodynamic point of view. We can however exclude models based on their dust content—  $A_2^{\text{ND}}$  and  $A_2^{\text{MW}}$  clearly have too little and too much dust, respectively, and there is tension between observations of dust in elliptical galaxies the high dust content of models  $A_2^{-3}$  and  $A_2^{\text{CE2}}$ .

Now we discuss the energetic aspects of black hole accretion. The next column illustrates a factor of  $\simeq 10$  spread in black hole growth by the end of the simulations. The mass growth is strongly correlated with the dust to gas ratio of the galaxy, with low dust models having more black hole growth. Dust grains, which have large UV absorption cross-sections, absorb UV photons and thus momentum from the luminous black hole. This radiative momentum in turn props up the gas, retarding its rate of accretion. Thus, the presence of dust tends to screen the black hole from accreting gas. Similarly, radiative feedback is able to more effectively terminate bursting events in models with more dust.

A simple check on the validity of a given model is whether the final black hole mass is consistent with the  $M_{\text{BH}} - \sigma$  relation or whether the final black hole mass is too large. Stellar evolution over a cosmological time releases an amount of gas into the galaxy equal to  $\simeq 30\%$  of the initial stellar mass. If more than  $\simeq 1\%$  of this gas were to be accreted, the  $M_{\text{BH}} - \sigma$  relation would be violated. The black hole growth in our models never exceeds  $\simeq 10^9 M_{\odot}$  (see Fig. 2, top panel), which preserves the Magorrian relation we assumed at the outset of the simulation.

The next three columns of Table 1 give the integrated effective luminosity in the indicated band in units of  $\Delta M_{\text{BH}} c^2$ . We recall that the adopted the electromagnetic efficiency of our simulations is ADAF-like, declining at low accretion rates and saturating to a prescribed value at high accretion rates. We use a saturation value of 0.125 (see CO07 Equation 33). Since the values of  $e_{\text{Bol}}$  are roughly constant and near the saturation value, the bulk of accretion must occur at high accretion rates independent of the dust treatment. However, the distribution into different bands is sensitive to dust due to opacity effects.

$e_{\text{UV}}$  indicates the amount of dust during periods of high quasar luminosity, so it is naturally maximal in the no dust model  $A_2^{\text{ND}}$ . The optical output tends to follow the UV in its overall behavior. The hard X-ray output is very similar in all models since the dust plays no part in its transmission. However, this component is slightly lower in the  $A_2^{\text{MW}}$  model since the maximal dust model emits a larger fraction of its energy at low Eddington ratios where the overall radiative efficiency is lower in the A type of models.

Two of the energy output columns allow us to discriminate cleanly among the models, eliminating those having observational properties inconsistent with known



data. One important ratio is that of the total quasar electromagnetic output to the observed AGN optical, as inferred by  $e_{\text{OP}}/e_{\text{Bol}}$ . This ratio, the “bolometric correction”, has been classically estimated to be in the range of 5 to 10 (Soltan 1982; Yu & Tremaine 2002). Richards et al. (2006) created composite SEDs of 249 quasars using photometry from Spitzer and the Sloan Digital Sky Survey. They measured a mean ratio of bolometric luminosity to total optical luminosity (integrated from 0.1 to 1  $\mu\text{m}$ ) of  $2.9 \pm 1.5$ , with values ranging between 1.8 and 19, and a bolometric correction to the 5100Å flux of  $10.3 \pm 2.1$ . Most of our models fall comfortably within the 5 -10 range, though the  $A_2^{\text{CE2}}$  and  $A_2^{-3}$  models have a bolometric correction exceeding 20.

Additionally, Richards et al. (2006) report an integrated IR flux between 1 and 100 $\mu\text{m}$  for their quasar sample, with no corrections made for the ISM of the host galaxy. The ratio of the mean bolometric luminosity to the integrated IR luminosity is  $2.58 \pm 0.75$ , and IR to optical ratio of  $1.3 \pm 1.5$ . These ratios spanned a range of 1.1 to 5.8 and 0.36 to 18, respectively. With the exception of the  $A_2^{\text{ND}}$  model, all models have total IR ( $e_{\text{IR}}$ ) exceeding total optical ( $e_{\text{OP}}$ ) by a factor greater than two and as much as 8.  $A_2^{\text{CE2}}$ ,  $A_2^{-4}$ , and  $A_2^{\text{MW}}$  have values closer to the mean. For the radiation output from the AGN itself, we have implicitly assumed a total IR to optical ratio of 1.2. Deviations from this value are due entirely to processing by the galaxy.

In Figures 4 and 5, we present the evolution of the effective optical luminosities of the black hole and stars, the total IR luminosity ( $L_{\text{IR}}$  from Table 1 plus a contribution from the central black hole), the Eddington fraction, and the black hole mass. The two figures consider separately models with constant dust to gas ratios and those where this ratio varies with time and radius. The top panel of Figure 5 shows the evolution of the  $A_2$  model taken from Ciotti et al. (2009b) with the improvements detailed in Section 3. The time evolution of each simulation has some variation from model to model, but the AGN activity of all models declines with cosmic time. This decline demonstrates how the main driver of secular evolution is the relative importance of mass injection (declining as  $\approx t^{-1.4}$ ) and supernova heating (declining as  $\approx t^{-1}$ ), so that the specific heating of the galaxy declines and galaxies develop a global wind. The sharpness of the bursts is due to the use of the A family of models, which have sharper bursts and shorter duty cycles than the B family. All differences above these general trends are due to the treatment of dust.

The duty cycles shown in the last column of Table 1 are somewhat shorter than the 0.01 typical of current observations. As previously discussed, 1D simulations have inherently less steady accretion due to the inability of the gas to fragment. Additionally, the A class of models has routinely produced short duty cycles due to its fixed efficiency for driving winds resulting in short duration bursts. In contrast, the more intricate B class of models, whose efficiency increases with increasing Eddington ratio, typically produced higher duty cycles (Ciotti et al. 2009b). We choose to use the A class for the purpose of this study as the accretion physics is cleaner and the role of the dust consequently easier to disentangle.

Figure 6 shows that in all models, most of the energy

is emitted at or above the Eddington limit. However, the amount of time spent at a given fraction of Eddington varies substantially among the dust models considered here, with very low duty cycles being typical. A very small fraction of the time in all models is spent above  $L_{\text{Edd}}$ . To gauge how much time each model spends in a quiescent phase, we also plot the amount of time spent below a given fraction of Eddington. Ho (2009) finds that roughly 50% of AGN have  $L_{\text{BH}}/L_{\text{Edd}} < 10^{-5}$ . As the dust content of the models goes down, the time spent at high Eddington fraction increases. This supports the idea that gas is more easily able to stream to the center of the galaxy in low dust models, resulting in sharp luminous bursts. In contrast, high dust models require more gradual buildup of cold dense shells of infalling gas before being able to overcome the radiative pressure exerted by the central black hole.

Aird et al. (2012) find that the probability density function of finding a galaxy with a specific Eddington ratio is well-described by a power law between Eddington fractions of  $10^{-4}$  and 1. We plot the corresponding cumulative distribution function for comparison in Figure 6 and find again that our 1D models spend too little time at Eddington ratios of  $10^{-4} - 10^{-1}$ . However, the data is in rough agreement with the simulations for very high Eddington ratios.

Taken together, these aspects of the models clearly identify those that are unphysical. The  $A_2^{\text{ND}}$  model produces too little IR emission while the  $A_2^{\text{MW}}$  produces too much. The standard  $A_2$  model at late times has very little IR output relative to optical, suggesting that its dust depletion is too great given its gas mass.  $A_2^{-4}$ , which it has similar levels of depletion, has an order of magnitude greater IR output as it also has roughly an order of magnitude more gas and therefore dust, bringing its value of  $L_{\text{IR}}/L_{\text{OP*}}$  closer to the observational value. However, the  $A_2^{-4}$  model does not have adequate dust to produce significant obscuration, which is inconsistent with high obscured fractions. Like the  $A_2^{-4}$  model, both models employing the continuity equation treatment of the dust abundance have a reasonable amount of IR emission, in addition to having sensible values for both the black hole mass and the duty cycle. In conclusion (and perhaps not surprisingly), the  $A_2^{\text{CE}}$  and  $A_2^{\text{CE2}}$  models pass the preliminary screenings better than the other models, and we will focus on these models in Section 5.

#### 4.1. Burst Behavior

Due to the relevance of the black hole accretion physics, we now discuss the burst behavior. Each burst begins with the formation of a cooling gas shell at  $\lesssim 1$  kpc from the center of the galaxy. In 1D simulations, this cold shell starts to fall toward the center and compresses the gas interior to it. As the gas density is increased, the black hole luminosity also increases. As soon as the black hole reaches  $\simeq 0.01L_{\text{Edd}}$ , pre-heating instabilities appear and the accretion becomes unstable with shock waves propagating toward the falling cold shell. Fresh material is carried to the black hole by reflected shock waves. The gas in the cold shell is compressed and star formation is induced. However, the piling up of cooling material from outside the shell pushes the cold material to the center. The accretion of this material produces a

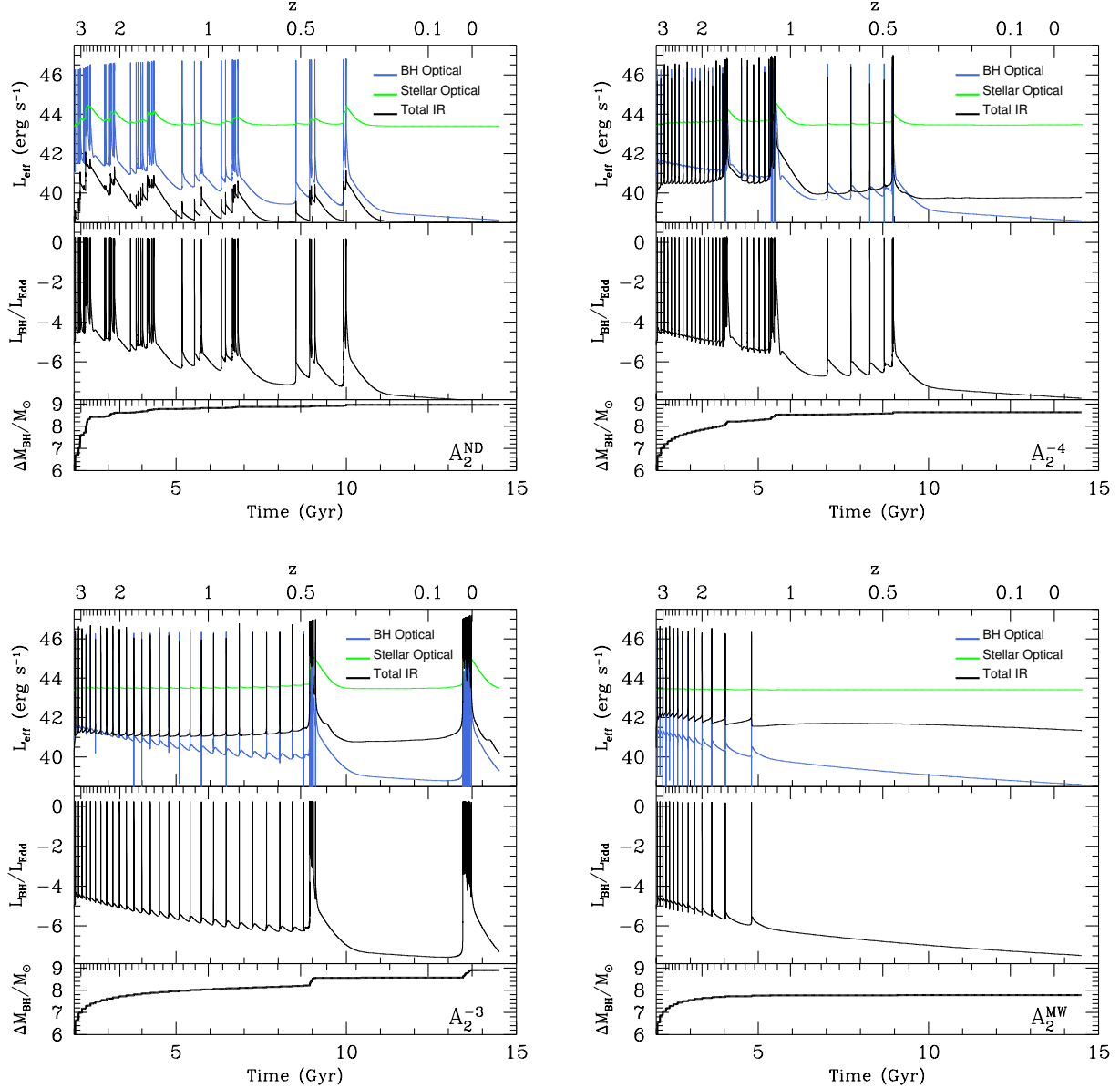


FIG. 4.— A comparison of the luminosity evolution for all models with constant dust to gas ratios. *Clockwise from top left:*  $A_2^{\text{ND}}$ ,  $A_2^{-4}$ ,  $A_2^{\text{MW}}$ , and  $A_2^{-3}$ . Each figure is organized as follows. *Top:* the luminosity seen at infinity in the optical from the black hole (blue) and the stars (green). The total IR luminosity, including the contribution from the central black hole, is plotted in black. *Middle:* The Eddington fraction, defined as the bolometric black hole luminosity divided by the Eddington luminosity. *Bottom:* The total black hole growth since the beginning of the simulation. All quantities are given as  $\log_{10}$ .

large final accretion event that quenches star formation.

This general evolution is naturally affected by gas opacity, which determines how well radiation pressure works against the falling shell. Therefore, it is not surprising that the details of each burst change with the different dust treatments.

Figure 7 demonstrates the effects of changing the dust content of the gas on the burst dynamics. One burst episode was selected from each model near 3 Gyr, then scaled such that the maximum  $L_{\text{BH}}/L_{\text{Edd}}$  occurs at  $\Delta t = 0$ . We note that the short few Myr duration of the bursts in these models are a feature of the A family of models, and that the more complicated B models have burst durations of  $\simeq 10$  Myr. While the common epoch

for the burst ensures some level of consistency in the galaxy evolution among models, the  $A_2^{\text{ND}}$  model has undergone significantly more black hole growth by this time than the other models, which must be taken into account when interpreting the results. For each model, we plot a number of relevant quantities that change through the burst— the X-ray luminosity of the hot ISM in the 0.38 keV band, the optical depth to the center of the galaxy in the optical band, the dust luminosity  $L_{\text{IR}}$ ,  $\langle T_d \rangle$  as described in 35, and the SFR.

Overall, the burst evolution follows the qualitative picture of the hydrodynamics given at the beginning of this section irrespective of dust treatment. The black hole luminosity rises rapidly followed by a decline due to the

TABLE 2  
IR DUTY CYCLE

Model	z: 3 - 2.5		z: 2.5 - 2		z: 2 - 1.5		z: 1.5 - 1		z: 1 - 0.5		z: 0.5 - 0	
$A_2^{\text{ND}}$	0.00	0.00	0.00	0.00	0.00	0.00	0.00	0.00	0.00	0.00	0.00	0.00
$A_2$	0.23	0.08	1.14	0.71	0.76	0.49	0.16	0.09	0.03	0.01	0.29	0.22
$A_2^{-4}$	0.31	0.10	0.22	0.07	0.75	0.46	1.33	0.47	0.04	0.01	0.07	0.05
$A_2^{\text{CE}}$	0.44	0.02	0.39	0.00	0.34	0.00	0.89	0.58	0.75	0.52	0.04	0.02
$A_2^{\text{CE2}}$	0.44	0.00	0.39	0.01	0.39	0.00	2.03	1.20	11.60	1.27	0.06	0.03
$A_2^{-3}$	0.46	0.13	0.36	0.12	0.22	0.06	0.18	0.06	0.15	0.05	5.19	0.91
$A_2^{\text{MW}}$	0.50	0.36	0.34	0.22	0.11	0.07	0.04	0.02	0.00	0.00	0.00	0.00

**Notes:** Each cell contains the percentage of time during a given redshift range that the galaxy has an IR luminosity comparable to LIRGs ( $10^{11} L_\odot$ , left) and ULIRGs ( $10^{12} L_\odot$ , right). In most models, phases of intense IR output have petered out below redshift  $\simeq 1$  and in nearly all by  $\simeq 0.5$ .

expansion of gas in the central region. Coincident with the peak in black hole luminosity are peaks in both  $L_{\text{IR}}$  and the star formation rate (SFR). Following this positive feedback on star formation, the SFR drops due to the AGN feedback.

There are small but important differences in the evolution among the models. The trends are best illustrated by the models with constant dust to gas ratios, as the changes are often monotonic with this ratio. For instance, the dustier models have a faster decline in black hole luminosity after the peak. The black hole is more effective in pushing gas away in models with more dust, which slows accretion. Similarly, the drop in SFR is monotonic in dust to gas ratio since feedback is faster and more effective in dustier models.

We now ask how this picture is modified when the dust abundance is treated in a more realistic way. The simplest physical treatment is the  $A_2$  model where the dust depletion is a simple function of temperature. The bursting behavior of this model is illustrated in the right-hand side of Figure 7. Prior to the burst, this model looks very much like the  $A_2^{\text{MW}}$  model since it has high values of  $\tau_{\text{OP}}$  and  $L_{\text{IR}}$ . After the burst, however, the AGN heats the gas in the galaxy, which, due to the temperature-dependent dust to gas ratio, instantaneously destroys the dust. Indeed, the  $A_2$  model closely resembles the  $A_2^{\text{ND}}$  model following the peak, notably in the slightly enhanced duration of the burst and its relative lack of suppressed star formation.

In the  $A_2^{\text{CE}}$  and  $A_2^{\text{CE2}}$  models, the dust must form and be destroyed on more realistic timescales. In the cold shells, the decreased temperatures allow for grain growth via collisions. From Figure 1, the grain growth time in a  $10^4$  K shell of cold gas with density  $10^3 \text{ cm}^{-3}$  is  $\simeq 0.01$  Myr, short enough to ensure the shell is dusty. However, if the shells do not reach these densities, the growth time can become long compared to the infall time, rendering the dust unable to affect the dynamics. This is in contrast to  $A_2$  in which cold gas would by assumption be immediately restored to MW-like grain abundances. Indeed, the right panel of Figure 7 has little evidence for enhanced dust for either the  $A_2^{\text{CE}}$  or  $A_2^{\text{CE2}}$  models, nor does the total dust mass plotted in Figure 3 show any evidence for enhancement during prior to  $\simeq 5$  Gyr despite many bursts. However, the existing dust is able to af-

fect the dynamics in ways comparable to the  $A_2^{-3}$  and  $A_2^{-4}$  models, notably more effective AGN feedback leading to shorter bursts and suppressed star formation. The mixing time in the  $A_2^{\text{CE2}}$  model does not appear to have noticeable effects on the hydrodynamics on the timescale of this burst.

By inspection of Figures 4 and 5, it is obvious that not all bursts are as sharp as that expanded in Figure 7. In general, a series of bursts culminates in a stronger final burst with considerably more time structure. These episodes are easily identified in Figures 4 and 5 as the thickest bands. We recall that in the B family of models, not discussed in this paper, the majority of bursts are of this kind. These bursts have longer duration during which a significant amount of material is accreted and are usually followed by long periods of quiescence for the galaxy. Models with little or no dust have correspondingly less radiative feedback from the AGN, and are thus characterized by short, clean bursts. In contrast, the dustier models have more long duration bursts as more material is allowed to build up and then accrete.

For illustration, in Figure 8 we expand the burst around 5 Gyr in model  $A_2^{\text{CE}}$  and give the Eddington fraction, effective optical luminosity from the black hole,  $\tau_{\text{OP}}$ ,  $L_{\text{IR}}$ ,  $\langle T_d \rangle$ , and the SFR through the burst. Note that the time axis in the left panel spans 150 Myr, while the right panel has the same 4 Myr span as in Figure 7.

In this model, the dust optical depth has sufficient time to rise above unity before being stopped by the dust-destroying AGN luminosity due to the buildup of a large, dense shell. Once the large structure is able to collapse, a cavity forms as the newly-fueled central AGN is able to drive out gas, dropping the accretion rate to effectively zero. In this time, gas will again accumulate until it becomes cool and dense enough to accrete. The galaxy oscillates between these modes for tens of Myr before returning to the equilibrium configuration, as illustrated in the left panel of Figure 8. Due to the prolonged existence and extreme density of the cold shell, grain growth becomes important, with spikes of grain growth evident in Figure 3 and the dust to gas ratio saturated in the cold shell evident in Figure 9. These dramatic bursts illustrate the close interplay between grain growth in cold shells and the radiation pressure that supports them.

While the two models employing the dust continuity

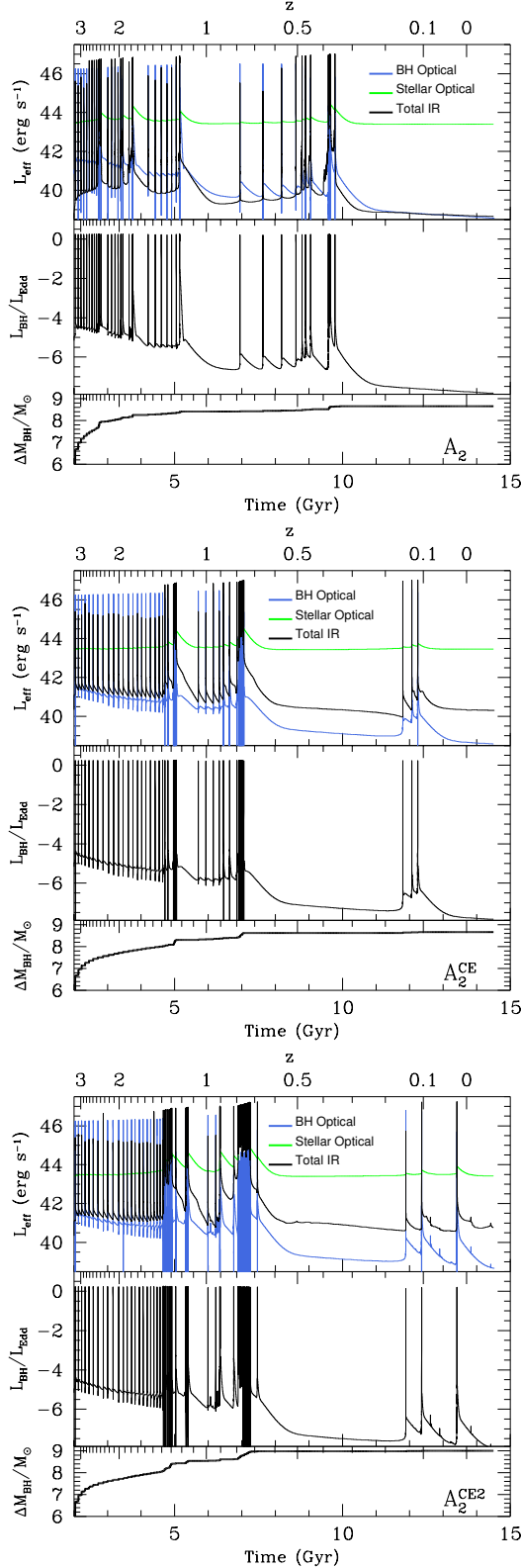


FIG. 5.— As in Figure 4, but for the  $A_2$  and continuity models which solve for the dust abundance as a function of radius. All three models have sharp continual bursts throughout the simulation as well as significant black hole growth, consistent with the models with low dust abundance.

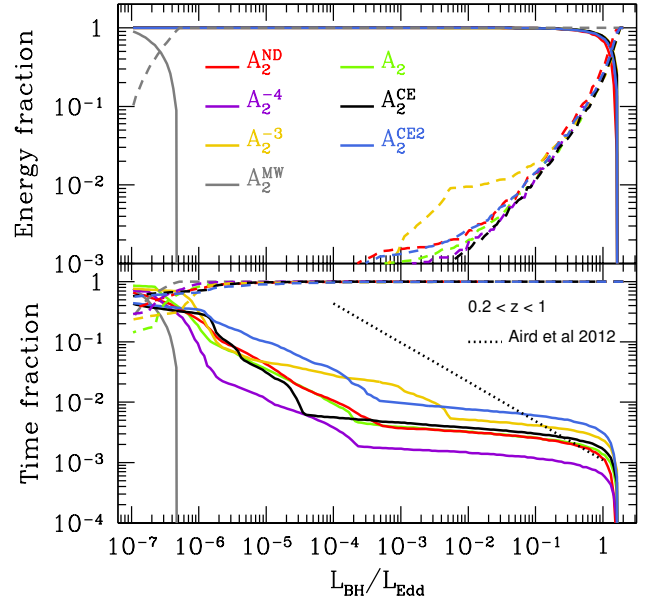


FIG. 6.— *Top*: The fraction of energy emitted above a given fraction of Eddington luminosity in the time interval  $0.2 < z < 1$ . *Bottom*: The fraction of time spent above a given fraction of Eddington luminosity. In both plots, we consider the bolometric black hole luminosity. For comparison, we plot the best-fit model of Aird et al. (2012) for the same time window.

equation have similar overall behavior, the “two stream” approach results in more burst of this nature. This can be attributed to the lag time between dust creation and mixing, which makes the AGN feedback less effective in the early stages of the burst before mixing can occur.

## 5. OBSERVATIONAL PROPERTIES OF MODELS

Each simulation discussed above can be assessed by its ability to reproduce the observed properties of elliptical galaxies containing supermassive black holes. Additionally, we can assess the importance of dust in the determination of each of the observational characteristics we present by analyzing the variation in these quantities among the simulations.

### 5.1. Dust in Quiescent ETGs

It is well-established that early type galaxies harbor very little dust due to rapid sputtering of grains in hot gas, with Clemens et al. (2010) putting an upper limit on grain lifetimes of  $46 \pm 25$  Myr. However, *Spitzer* and *Herschel* have enabled study of the dust that is present and are providing important clues on the origin of that dust. Here we summarize some recent results on the dust in elliptical galaxies and compare with our simulations.

The *Herschel* Virgo Cluster Survey detected dust emission in 46 of 910 ETGs in their sample (di Serego Alighieri et al. 2013), with total dust masses ranging between  $7 \times 10^4$  and  $1.1 \times 10^7 M_\odot$ . They further note that these masses are greater than expected for a passively evolving galaxy, and cite a potential external origin for the dust.

The *Herschel* Reference Survey performed a similar study on 62 ETGs, detecting dust in 31 (Smith et al.

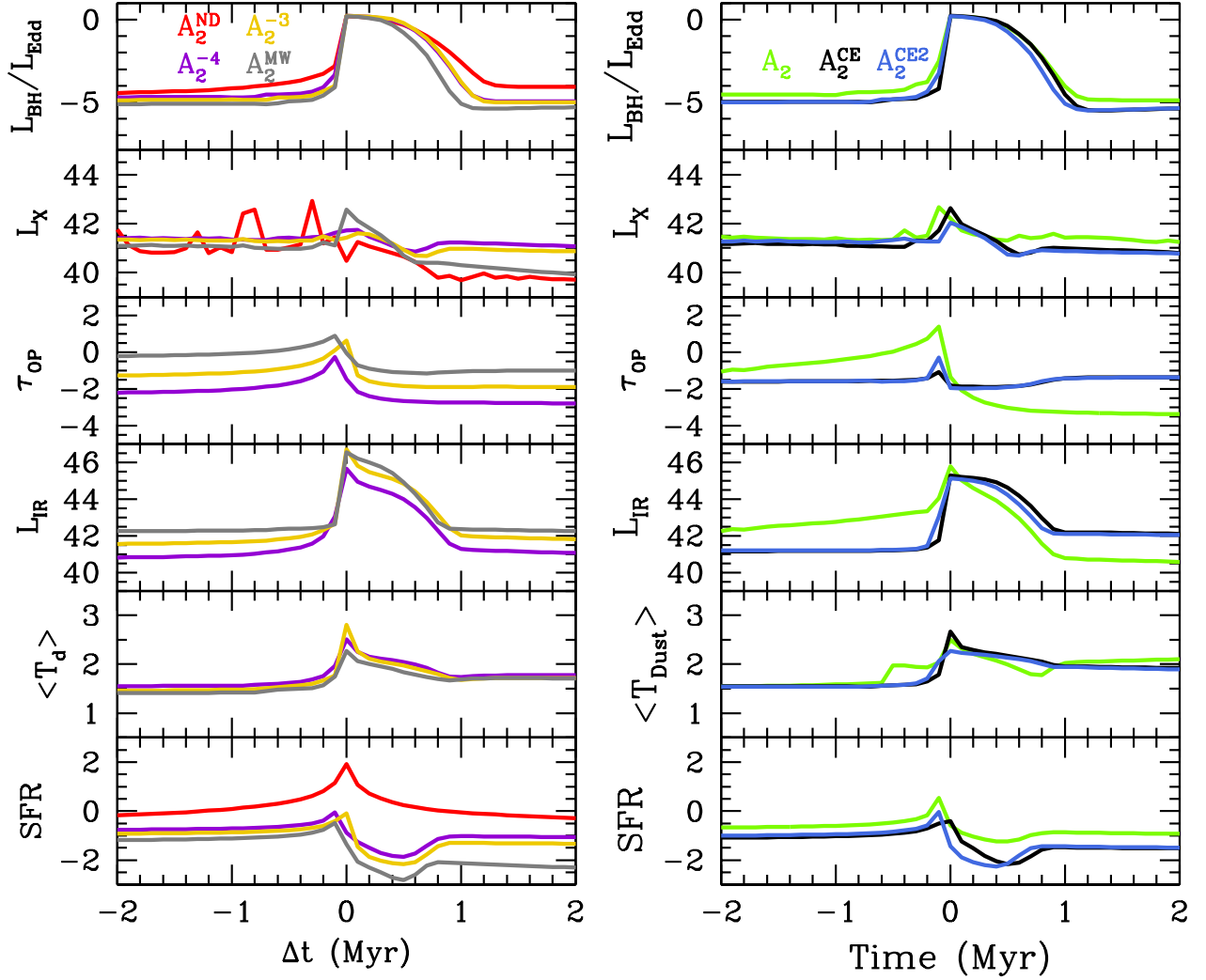


FIG. 7.— *Left Panels:* Time evolution of relevant quantities during a burst in models with constant dust to gas ratios. For each model, a burst was selected near 3 Gyr and scaled such that the maximum  $L_{\text{BH}}/L_{\text{Edd}}$  occurs at  $\Delta t = 0$ . We plot  $A_2^{\text{ND}}$  in red,  $A_2^{-4}$  in violet,  $A_2^{-3}$  in gold, and  $A_2^{\text{MW}}$  in gray. From top to bottom, the panels give the X-ray luminosity in the 0.38 keV band from the hot emitting ISM in erg/s, the optical depth to the center of the galaxy in the optical band, the dust luminosity in erg/s, the luminosity-weighted dust temperature (see Equation 35) in K, and the star formation rate in  $M_\odot/\text{yr}$ . All y-axis quantities are given as  $\log_{10}$ . Note that the  $A_2^{\text{ND}}$  model is not plotted in the  $\tau_{\text{OP}}$ ,  $L_{\text{IR}}$ , and  $\langle T_d \rangle$  panels since it has no dust and thus a value of zero for each of these quantities. *Right Panels:* Same as Left, but for models with dust to gas ratios that vary with time and radius.  $A_2$  is plotted in green,  $A_2^{\text{CE}}$  in black, and  $A_2^{\text{CE2}}$  in blue.

2011). They too find that the dust masses exceed predictions for passively evolving galaxies after accounting for sputtering in hot gas, and posit that the excess dust may be the result of mergers. Both studies find a lack of correlation between the dust mass and stellar mass, casting doubt on the hypothesis that the dust originates solely from stellar outflows.

Using far-infrared *Spitzer* data, Temi et al. (2007a) analyzed the SEDs of 46 elliptical galaxies, finding large ( $\sim 100$ ) variations in  $70 \mu\text{m}$  and  $160 \mu\text{m}$  luminosity even for ellipticals with the same B-band luminosity. Six galaxies showed extended  $70 \mu\text{m}$  emission that was in excess of what would be predicted by dust production and sputtering rates. Further, none of the galaxies showed

evidence of recent mergers and indeed some had quite old stellar populations. Observing dust emission as extended as 5 - 10 kpc, the authors suggest that the dust has been buoyantly transported out from a dusty nuclear region on a timescale less than the sputtering time.

Martini et al. (2013) use *Spitzer* observations of 38 ETGs to conclude that ETGs without dust lanes tend to have less than  $10^5 M_\odot$  of dust. Additionally, like di Serego Alighieri et al. (2013) and Smith et al. (2011), there is a large scatter in the inferred dust mass at a fixed stellar mass. Like Temi et al. (2007a), they conclude that mergers cannot alone count for the excess dust as the expected merger rate is too slow relative to the dust destruction time. They propose instead that grain growth

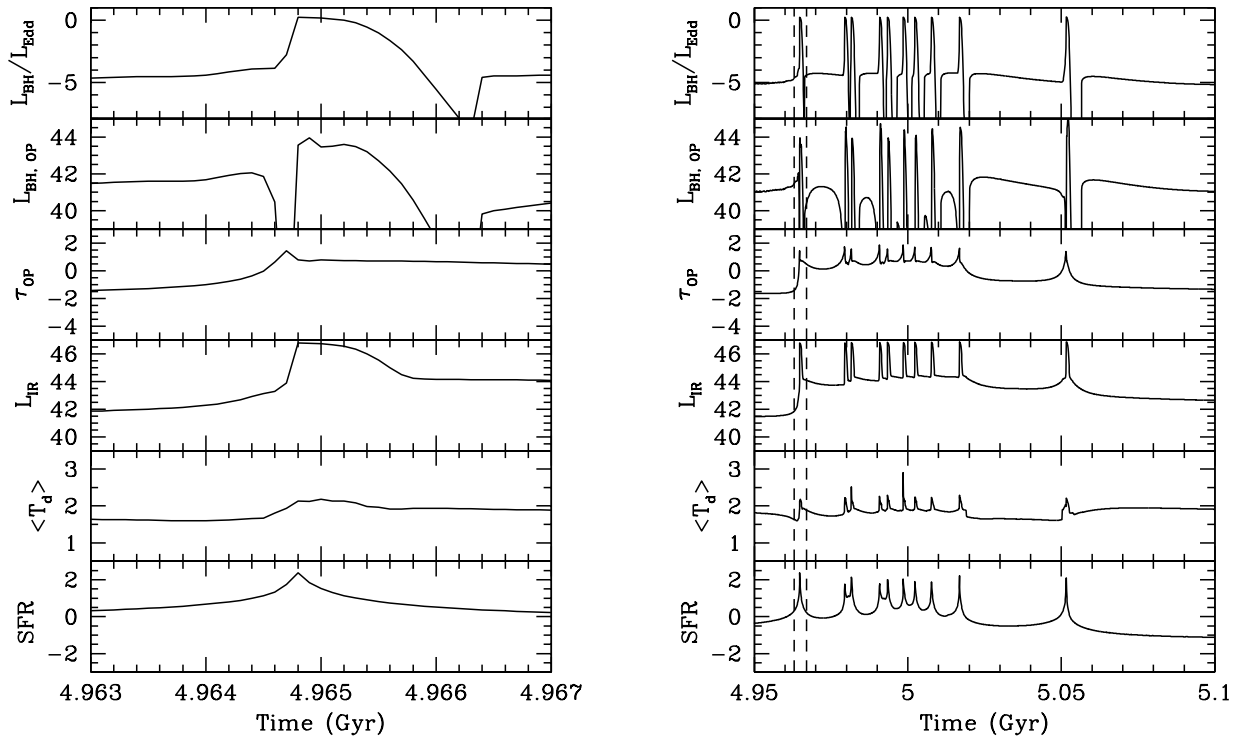


FIG. 8.— A major accretion event in the  $A_2^{\text{CE}}$  model. We present the first 4 Myr (the same time scale as Figure 7) of this burst in the left panel, and 150 Myr evolution of this burst in the right panel with the time limits of the right panel indicated by dashed lines. From top to bottom, we give the Eddington fraction, the effective optical luminosity of the black hole, the optical depth in the optical band, the IR luminosity from radiation reprocessed by dust, the emission-weighted temperature, and the star formation rate in  $M_\odot/\text{yr}$ . All y-axis quantities are given as  $\log_{10}$ .

can occur in externally accreted cold gas, with the enhanced lifetimes of the dust in the cold gas sufficient to explain the excess.

In our continuity models, which do not include any non-secular processes such as mergers or accretion of cold gas from the IGM, dust growth is able to occur in the cold gas produced by cooling flow instabilities. The presence of such gas is attested by multi-wavelength observations of giant ellipticals, revealing a cold ISM component (Werner et al. 2013). In the  $A_2^{\text{CE}}$  model in particular, the dust to gas ratio at  $z = 0$  is a typical  $10^{-4}$  while the dust mass is  $\simeq 10^6 M_\odot$ , values in accord with (Smith et al. 2011). Thus, our most detailed model is able to reconcile observations with theoretical estimates of dust production and destruction rates.

Additionally, the  $A_2^{\text{CE}}$  and  $A_2^{\text{CE2}}$  models predict that the distribution of dust in a quiescent galaxy (see Figure 9, left panel) that is concentrated within the inner 100 pc and then sharply declining. Although the right panel of Figure 9 is a snapshot of the radial profile in the midst of a complex burst, the AGN luminosity at that precise time (see Figure 8) is very low, and thus this object too would be interpreted as quiescent. The dust distribution of the galaxy at this time is markedly different, with high dust to gas ratios seen out to  $\simeq 10$  kpc scale, similar to what is observed by Temi et al. (2007a,b).

Finally, our models also anticipate a large variation in  $L_{\text{IR}}$  while  $L_{\text{OP*}}$  remains relatively fixed. In Figure 10 we give the histogram of the infrared dust luminosity

in equally-spaced time intervals over the simulation. In both the  $A_2^{\text{CE}}$  and  $A_2^{\text{CE2}}$  models, the typical dust luminosity varies between  $\simeq 10^{40} - 10^{42}$  erg/s.

The dust distribution predictions of our  $A_2^{\text{CE}}$  and  $A_2^{\text{CE2}}$  models lends itself to a simple observational test. Because the dust abundance declines sharply with radius, we find the ratio of the half radii of the IR emission from dust and X-ray emission from the hot ISM to be  $\simeq 0.2$  in these models. In contrast, this ratio has a value of  $\simeq 1$  in models with constant dust to gas ratios.

## 5.2. Dust in Galaxies with AGN

A generic feature of all of our models is that the luminosity-weighted dust temperature increases dramatically during bursts, usually exceeding 100 K and often approaching the grain sublimation temperature of  $\simeq 1200$  K for a brief period. This is due to the intense AGN luminosity heating grains in the infalling cold gas as well as the interior of the galaxy. A key test of the viability of our models is the presence of a significant hot dust component to the total infrared luminosity during AGN on phases.

Using data from the AKARI Mid-Infrared Survey, Oyabu et al. (2011) discovered two LIRGs obscured in the optical but showing strong thermal dust emission in the IR. The derived dust temperatures were in excess of 500 K for a hot component and 93 K for a dominant cool component with total IR luminosity was on the order of  $10^{11} L_\odot$ . Both objects were interpreted as obscured

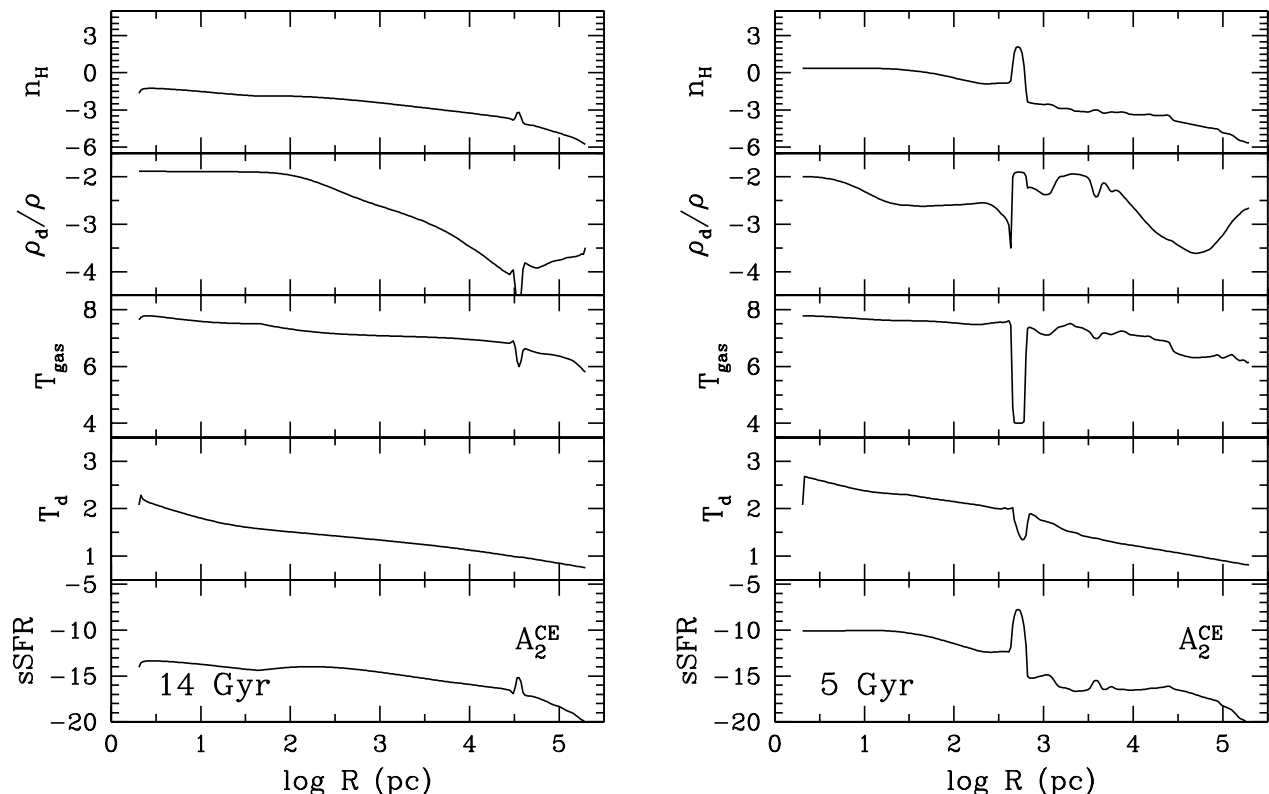


FIG. 9.— The radial profile of the  $A_2^{\text{CE}}$  model at 5 and 14 Gyr. At 5 Gyr, the galaxy is in a prolonged period of high optical depth and bursting activity (see Figure 8), while at 14 Gyr it is quiescent. The panels are organized as follows, from top to bottom: the gas number density in  $\text{cm}^{-3}$ ; the dust to gas ratio; the gas temperature in K; the dust temperature in K; the specific star formation rate in  $\text{M}_{\odot}/\text{yr}/\text{pc}^3$ . All quantities are given as  $\log_{10}$ . The presence of a cold dense shell is evident at  $\simeq 500$  pc. Due to the star formation activity, the dust abundance is relatively high in the inner parts of the galaxy at 5 Gyr. Even at 14 Gyr, the galaxy maintains a high dust to gas ratio in the inner 100 pc.

AGN, which is broadly consistent with the predictions of our models during obscured phases.

A key observational test of our most detailed models is the presence of warm dust ( $T_d \simeq 100$  K) at  $\leq 1$  kpc during burst events (see Figure 8, right panel). This dust is associated with the cold, dense gas that fuels the central black hole, and while it is not close enough to the central AGN to be heated to the sublimation temperature of grains, it is close enough to be heated to temperatures higher than expected in the ISM of a quiescent galaxy.

### 5.3. Obscured Fraction

Mayo & Lawrence (2013) and Lawrence & Elvis (2010) find that only roughly 1/3 of AGN are unobscured. We assess the “obscured fraction” in our models by considering how much time of the AGN-loud phase is spent at high  $\tau_{\text{OP}}$ . We choose the natural threshold of  $\tau_{\text{OP}} > 1$  to deem the AGN “obscured,” which assuming a constant dust to gas ratio of  $10^{-4}$  implies a column density of  $2 \times 10^{23} \text{ cm}^{-2}$  given our prescription for  $\kappa_{\text{OP}}$  (Equation 2). For the continuity model, we find that  $\tau_{\text{OP}} > 1$  for 54% of the time that the AGN is on ( $L_{\text{BH}}/L_{\text{Edd}} > 1/30$ ), the two-stream 73%, the standard  $A_2$  model 44%, the constant  $10^{-2}$  depletion model 10%, and the model with MW dust abundance 3%. It is clear that to obtain the observed high obscuration fractions it

is necessary to decouple the dust abundance from the gas abundance—models with too much dust cannot sustain accretion and high Eddington ratios while models with little dust provide minimal obscuration. Only by allowing the dust to be formed and destroyed in a physical way do we see the emergence of clear obscured and unobscured phases directly related to the ability of the AGN to drive and quench star formation, and consequently dust production.

### 5.4. Star Formation Rate

As already described in CO07, all of our models predict a period of AGN-induced star formation, the so-called “positive feedback” Ishibashi & Fabian (seealso 2012); Zubovas et al. (seealso 2013), with star formation occurring within the inner few hundred parsecs in the galaxy. Following this period, star formation is quenched to below pre-burst levels. Though the interplay is complex, it is evident that the black hole accretion rate (BHAR) and the star formation rate (SFR) are closely entwined.

Chen et al. (2013) sought evidence of a BHAR-SFR relationship by studying the *average* BHARs of AGN as determined by their X-ray luminosity and looking for correlations with the SFR as inferred from the IR luminosity. Due to the intense variability of AGN on timescales short compared to star formation time, averaging is em-



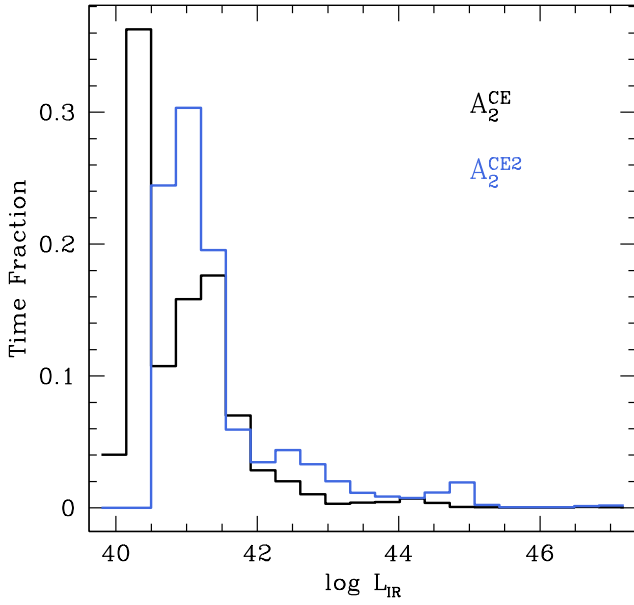


FIG. 10.— The IR luminosity from dust from 125,000 equally-spaced time slices in the simulation versus the time fraction spent in each luminosity bin. The majority of the time, both the  $A_2^{\text{CE}}$  (black) and  $A_2^{\text{CE2}}$  (blue) have IR luminosities within a range  $\simeq 10^{40} - 10^{42}$  erg/s. Observations likewise indicate a large scatter in IR luminosity even for ellipticals at fixed stellar mass.

phasized as painting a clearer picture of the relationship. They find that

$$\log(L_X[\text{erg/s}]) = 30.37 + 1.05 \log(L_{\text{IR}}/L_{\odot}) \quad , \quad (40)$$

for their best-fit model, which analyzed galaxies in the redshift range  $0.25 < z < 0.8$  and with SFRs  $0.85 < \log \text{SFR}/M_{\odot} < 2.56$ . Converting to BHAR and SFR, they obtain

$$\log \text{BHAR} = -3.72 + 1.05 \log \text{SFR} \quad . \quad (41)$$

To compare this result with our most physical simulated galaxies, in Figure 11 we make the same cuts in redshift and SFR and consider the BHAR and SFR in the simulation at equally-spaced times. Since the observational data do not have objects with  $L_X > 10^{44}$  erg/s, and since these objects are likely to be obscured in our simulations at variance with the  $10^{20} \text{ cm}^{-2}$  column density assumed by Chen et al. (2013), we removed all points with  $L_X > 10^{44}$  erg/s.

Indeed, there is a strong linear correlation in all models between the BHAR and SFR. However, the points cluster more closely to the line  $\text{BHAR} = \text{SFR}/500$ , which Chen et al. (2013) derived from the  $M_{\text{BH}}\text{-}M_{\text{bulge}}$  relations of Marconi et al. (2004) than to the observations of Chen et al. (2013). Nevertheless, the slopes appear consistent. The  $L_X\text{-}L_{\text{IR}}$  plot varies significantly from the BHAR-SFR plot for our models. This could be partially due to rapid variations in the X-ray luminosity at relatively constant  $L_{\text{IR}}$ , to which the  $A_2^{\text{CE2}}$  model would be particularly susceptible given its delayed dust mixing. Averaging would bring the data into closer agreement with the observations.

It must also be noted that our models consider only AGN-induced star formation, and thus by neglecting star formation induced by other processes, e.g. mergers, we are likely under-predicting the total star formation rate. Secondly, we are modeling a single galaxy with a single velocity dispersion, not an ensemble of galaxies, so a quantitatively exact comparison is beyond the scope of this work. These caveats notwithstanding, AGN-induced star formation appears at least roughly consistent with the observed SFR-BHAR correlation.

## 6. DISCUSSION AND CONCLUSIONS

By implementing a more physically-based dust treatment into 1D hydrodynamical simulations of the evolution of massive elliptical galaxies, we are able to link the computed IR emission from the galaxy during various stages of secular evolution with observations of IR emission. These models are capable of attaining LIRG and ULIRG-like phases of high IR emission without needing to invoke non-secular processes.

Despite the differing assumptions on dust abundance, the simulated galaxies illustrated a remarkably robust mass budget— in each simulation, the vast majority of the gas in the galaxy was expelled in outflows, about 10% was turned into stars, a few percent was accreted onto the central black hole, and a few percent remained as gas. The black hole growth is consistent both with current determinations of the Magorrian relation and the empirical fact that quasar “on” periods decline in frequency with decreasing redshift.

Our most physical dust models are able to reconcile the low observed dust abundance of quiescent galaxies (dust to gas ratios of  $\simeq 10^{-4}$ ) with presence of heavily obscured quasars through grain growth and reduced sputtering rates in cold gas. Additionally, optically-thick gas was able to oscillate between accretion and outflow phases for tens of Myr, resulting in sustained periods of large IR luminosity consistent with LIRGs and ULIRGs. However, at variance with Debuhr et al. (2011),  $\tau_{\text{IR}}$  never exceeds unity and the momentum imparted to the dust gas never exceeds  $L_{\text{BH}}/c$ .

We identify two distinct types of AGN bursts common to all models— short-duration optically thin bursts that eventually culminate to a single large, complex burst that is largely optically thick. A clear prediction of this work is the presence of infrared emission from  $\simeq 100$  K dust grains in the inner  $\simeq 1$  kpc of massive galaxies during AGN bursts.

The presence of dust grains in accreting gas was also found to impact the star formation processes in the galaxy— AGN feedback and consequent quenching of star formation was enhanced in models with more dust. Similarly, dusty models also accrete less gas and have shorter duration bursts. Irrespective of our dust treatment, we find periods of “positive feedback” on star formation in which AGN activity precipitates a brief period of active star formation.

An inherent limitation of 1D simulations is the inability to account for fragmentation of gas. The influence of dust in this case, particularly in its role of preventing gas from accreting, has yet to be determined using a detailed physical prescription for the dust abundance. The formalism laid out in this work can be easily generalized to higher dimensional simulations, and given the



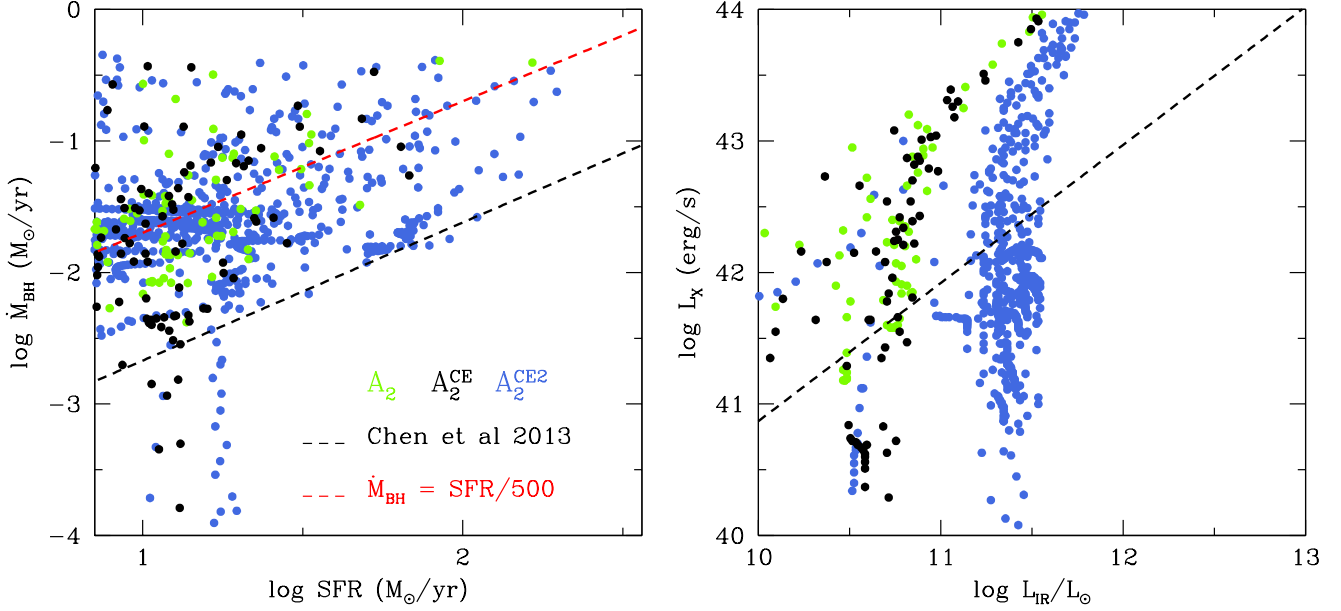


FIG. 11.— The correlation between the black hole accretion rate (BHAR) and the star formation rate (SFR) between redshifts 0.25 and 0.8. Both observations by Chen et al. (2013) and the simulations find a power law relationship with index of  $\simeq 1$ . The picture is less clear when looking at  $L_X$  and  $L_{IR}$ , the more fundamental observables, due to variations in  $L_X$  at fixed  $L_{IR}$ . Averaging improves agreement with observations.

importance of dust not only in the dynamics but also observational signatures, doing so may shed additional light on evolution of these galaxies.

We thank Bruce Draine, Jenny Greene, Jill Knapp, and Greg Novak for helpful discussions. BH acknowledges

support from the National Science Foundation Graduate Research Fellowship under Grant No. DGE-0646086. LC is supported by the grant MIUR 2008, and PRIN MUIR 2010-2011, project “The Chemical and Dynamical Evolution of the Milky Way and Local Group Galaxies” 2010LY5N2T.

#### REFERENCES

- Aird, J., et al. 2012, *ApJ*, 746, 90  
 Begelman, M. C., Blandford, R. D., & Rees, M. J. 1984, *Reviews of Modern Physics*, 56, 255  
 Binney, J., & Tabor, G. 1995, *MNRAS*, 276, 663  
 Boroson, B., Kim, D.-W., & Fabbiano, G. 2011, *ApJ*, 729, 12  
 Bregman, J. N., & Parriott, J. R. 2009, *ApJ*, 699, 923  
 Canizares, C. R., Fabbiano, G., & Trinchieri, G. 1987, *ApJ*, 312, 503  
 Cattaneo, A., et al. 2009, *Nature*, 460, 213  
 Chen, C.-T. J., et al. 2013, *ApJ*, 773, 3  
 Choi, E., Naab, T., Ostriker, J. P., Johansson, P. H., & Moster, B. P. 2013, *ArXiv e-prints*  
 Choi, E., Ostriker, J. P., Naab, T., & Johansson, P. H. 2012, *APJ* submitted  
 Ciotti, L., Morganti, L., & de Zeeuw, P. T. 2009a, *MNRAS*, 393, 491  
 Ciotti, L., & Ostriker, J. P. 1997, *ApJ*, 487, L105  
 —. 2007, *ApJ*, 665, 1038  
 Ciotti, L., & Ostriker, J. P. 2012, in *Astrophysics and Space Science Library*, Vol. 378, *Astrophysics and Space Science Library*, ed. D.-W. Kim & S. Pellegrini, 83  
 Ciotti, L., Ostriker, J. P., & Proga, D. 2009b, *ApJ*, 699, 89  
 —. 2010, *ApJ*, 717, 708  
 Clemens, M. S., et al. 2010, *A&A*, 518, L50  
 Coker, C. T., Thompson, T. A., & Martini, P. 2013, *ArXiv e-prints*  
 Debuhr, J., Quataert, E., & Ma, C.-P. 2011, *MNRAS*, 412, 1341  
 Di Matteo, T., Springel, V., & Hernquist, L. 2005, *Nature*, 433, 604  
 di Serego Alighieri, S., et al. 2013, *A&A*, 552, A8  
 Draine, B. T. 2011, *Physics of the Interstellar and Intergalactic Medium* (Princeton, NJ: Princeton University Press)  
 Draine, B. T., & Salpeter, E. E. 1979, *ApJ*, 231, 438  
 Ho, L. C. 2009, *ApJ*, 699, 626  
 Ishibashi, W., & Fabian, A. C. 2012, *MNRAS*, 427, 2998  
 Kemper, F., Stark, R., Justtanont, K., de Koter, A., Tielens, A. G. G. M., Waters, L. B. F. M., Cami, J., & Dijkstra, C. 2003, *A&A*, 407, 609  
 Kim, D.-W., & Pellegrini, S., eds. 2012, *Astrophysics and Space Science Library*, Vol. 378, *Hot Interstellar Matter in Elliptical Galaxies*  
 Knapp, G. R. 1985, *ApJ*, 293, 273  
 Lawrence, A., & Elvis, M. 2010, *ApJ*, 714, 561  
 Marconi, A., Risaliti, G., Gilli, R., Hunt, L. K., Maiolino, R., & Salvati, M. 2004, *MNRAS*, 351, 169  
 Martini, P., Dicken, D., & Storchi-Bergmann, T. 2013, *ApJ*, 766, 121  
 Mathis, J. S., Rumpl, W., & Nordsieck, K. H. 1977, *ApJ*, 217, 425  
 Mayo, J. H., & Lawrence, A. 2013, *MNRAS*  
 Nayakshin, S., & Zubovas, K. 2012, *MNRAS*, 427, 372  
 Norman, C., & Scoville, N. 1988, *ApJ*, 332, 124  
 Novak, G. S., Ostriker, J. P., & Ciotti, L. 2012, *ArXiv e-prints*  
 Ostriker, J. P., Choi, E., Ciotti, L., Novak, G. S., & Proga, D. 2010, *ApJ*, 722, 642  
 Ostriker, J. P., & Ciotti, L. 2005, *Royal Society of London Philosophical Transactions Series A*, 363, 667  
 Oyabu, S., et al. 2011, *A&A*, 529, A122+  
 Pellegrini, S., Ciotti, L., & Ostriker, J. P. 2012, *ApJ*, 744, 21  
 Raimundo, S. I., Fabian, A. C., Bauer, F. E., Alexander, D. M., Brandt, W. N., Luo, B., Vasudevan, R. V., & Xue, Y. Q. 2010, *MNRAS*, 408, 1714  
 Richards, G. T., et al. 2006, *ApJS*, 166, 470  
 Shin, M.-S., Ostriker, J. P., & Ciotti, L. 2010, *ApJ*, 711, 268  
 Siebenmorgen, R., & Heymann, F. 2011, *ArXiv e-prints*  
 Smith, M. W. L., et al. 2011, *ArXiv e-prints*

- Socrates, A., & Sironi, L. 2013, *ApJ*, 772, L21
- Soltan, A. 1982, *MNRAS*, 200, 115
- Springel, V., Di Matteo, T., & Hernquist, L. 2005, *MNRAS*, 361, 776
- Tem, P., Brighenti, F., & Mathews, W. G. 2007a, *ApJ*, 660, 1215
- . 2007b, *ApJ*, 666, 222
- Thompson, T. A., Quataert, E., & Murray, N. 2005, *ApJ*, 630, 167
- Vasudevan, R. V., Fabian, A. C., Mushotzky, R. F., Meléndez, M., Winter, L. M., & Trippe, M. L. 2013, *MNRAS*, 431, 3127
- Vogelsberger, M., Genel, S., Sijacki, D., Torrey, P., Springel, V., & Hernquist, L. 2013, ArXiv e-prints
- Weingartner, J. C., Draine, B. T., & Barr, D. K. 2006, *ApJ*, 645, 1188
- Werner, N., et al. 2013, ArXiv e-prints
- Yu, Q., & Tremaine, S. 2002, *MNRAS*, 335, 965
- Zubovas, K., Nayakshin, S., King, A., & Wilkinson, M. 2013, *MNRAS*, 433, 3079